Lucas Timotheo Sanches

Energy Extraction and Quasinormal Modes of Black Hole Binaries: An analytical and numerical study

Thesis presented to the Post-Graduation
program in Physics of Federal University of
ABC as a requirement for obtaining the title of
Doctor in Physics.

Advisor: Prof. Dr. Maurício Richartz

Santo André - SP

2022

AGRADECIMENTOS, DEDICATÓRIA, ETC...

Abstract

ABSTRACT HERE.

Keywords: Black Holes, Penrose Process, Energy Extraction, Quasinormal Modes

Resumo

RESUMO AQUI.

Palavras-chave: Buracos Negros, Processo de Penrose, Extração de Energia, Modos Quasinormais

Contents

Chapter 1

Introduction

One of the most well know predictions of the Theory of General Relativity (GR) is the existence of spacetime oscillations that propagate throughout the universe, the so called, gravitational waves. The first (indirect) evidence of the existence of such waves occurred when Hulse and Taylor observed, in 1975, the binary system PSR B1913+16 [1]. Observational data proved to be compatible with theoretical analysis for neutron star binaries that emit gravitational waves. On the other hand, direct observations, despite being attempted since the 1960s, only became a reality recently in the year 2015, with measurements from the Advanced Laser Interferometer Gravitational-wave Observatory (Advanced LIGO) [2, 3] giving birth to a new era in astronomy and cosmology. These two observations have a common factor: they involve *binary systems*, that is, two astronomical objects that are close enough for their mutual gravitational attraction to cause them to orbit around a common center of mass as they get closer and closer until a catastrophic collision event occurs, releasing huge amounts of energy and angular momentum in the form of gravitational radiation.

So far, no analytic description of a binary system in GR is known. This is due to the extreme complexity of Einstein's equations (a system of 10 coupled non-linear partial differential equations) whose exact solution is known only for very specific systems with a high degree of symmetry. Even if such an exact solution were to be found, it would likely be too large, complicated and impractical to use. Given that in a collision event the nonlinear character of the

equations becomes important the problem must be treated numerically, with the techniques of the field of Numerical Relativity (NR).

The main goal of our work is to study certain effects in GR that are well-know to spacetimes containing a single astrophysical object (a star or a black hole), namely the *quasinormal ringdown* and *the Penrose process*, and extend them to binary systems. To that end, we will work on two fronts: The first is a *semi-analytic* approach in which we will study exact (and analytic) solutions of Einstein's field equations that approximate binary black hole systems in static equilibrium. Such solutions allow us to employ well established numerical and semi-analytic techniques in our studies. The second is a *numeric* approach in which we will use non-exact approximations of binary systems that are no longer in static equilibrium for our investigations.

Chapter 2

Energy Extraction From Black Hole Binaries

2.1 Chapter Introduction

In this chapter, we will explore energy extraction from black hole binaries via the Penrose mechanism (also known as the Penrose Process, which we shall abbreviate respectively as PM and PP) in black hole binaries.

The first incarnation of the PM arose as a consequence of the Kerr metric. The Kerr metric is the best know mathematical description of rotating black holes given by the theory of General Relativity [4, 5, 6, 7]. Unlike static black holes, a Kerr black hole is characterized by the existence of a very peculiar region around its event horizon, known as the *ergosphere* or *ergoregion*. Particles that reach the ergosphere can still avoid the event horizon and, hence, are not doomed to end at the spacetime singularity. Nevertheless, any observer lying inside the ergosphere is unavoidably dragged along by the rotational motion of the black hole.

Particles inside the ergosphere may have negative energies (according to a static observer at infinity). Relying on this property, Penrose and Floyd devised a mechanism that allows one to extract energy from a rotating black hole [8]. The idea consists in sending a particle from infinity towards the black hole and assumes that, once inside the ergosphere, it decays into two other particles. If

one of the fragments is counter-rotating with the black hole and has negative energy (which implies that the split happens inside the ergosphere), it will be captured by the black hole, meaning that the other fragment will escape to infinity. Due to the conservation of the four-momentum, the escaping fragment will have more energy and more angular momentum than the incident particle. Rotational energy and angular momentum are, thus, effectively extracted from the black hole.

Our main motivating factor for this investigation was that despite being a well-known process, the PP had not been studied in the context of black hole binaries. We have also found that many recent research endeavors attempt to establish a relation of the PP with observable astrophysical phenomena. The collisional version of the process, for instance, considers multiple particles that collide and scatter in the ergoregion, allowing arbitrarily high center-of-mass energies. This process can potentially act as a mechanism to eliminate dark matter particles near a supermassive black hole [9]. The magnetic Penrose process [10, 11], on the other hand, considers charged particles and black holes surrounded by magnetic fields (originated, for instance, by plasma accretion disks around the black hole). The electromagnetic interaction allows for highly efficient energy extraction schemes, such as the one introduced in Ref. [12] to model the emission of ultra-high energy cosmic rays from supermassive black holes. Furthermore, recent numerical simulations of plasma and jets around Kerr black holes indicate the important role that negative energy particles and the Penrose process play on the total energy flux coming from the black hole's jets [13].

A few comments on the models chosen for representing the binary systems are in order. Firstly, the nomenclature that we use to refer to a BBH is as follows:

Definition 2.1.1 (Static/Dynamic BBH model). *A **static** BBH model represents two black holes that **do not** fall towards each other or move in any other way, thus remaining within a fixed location as time passes. This is in contrast to a **dynamic** BBH model, in which the constituent BHs either collide or move.*

Definition 2.1.2 (Exact/Approximate BBH model). *An **exact** BBH model is one that is an exact vacuum solution of Einstein's field equations. An **approximate** BBH*

model is one that is not and exact vacuum solution of said equations, and the deviation from vacuum is not considered to be an exotic type of matter but a measure of it's "non-exactness".

Definition 2.1.3 (Analythic/Numeric BBH model)**.** *An **analytic** BBH model is one whose entire spacetime metric is analytically known at all points and times. In contrast, a **numeric** BBH model is obtained only at a certain coordinate time hypersurface (typically t = 0) by solving the ADM constraint equations for a vacuum configuration numerically. Note that even tough such numerical solutions contain errors, and thus do not strictly solve the vacuum field equations (giving rise to constraint violations), we do not consider these to be approximate, since it's possible (at least in theory but not in practice due to physical limitation of machines and computational resources) to obtain these solutions with arbitrarily small constraint violations given that they are convergent.*

Secondly, any study that aims to model astrophysical binary systems must acknowledge the fact that there is no known exact and analytical solution of Einstein's equations describing such a system. Even if exact numerical or approximate analytical solutions are employed, the resulting spacetime metrics are non-stationary and thus limiting the applicability of the standard concept of an ergosphere. Recognizing these difficulties, we have utilized BBH models that are static, exact and analytic.

Our first task was to investigate the possibility of energy extraction from the Majumdar-Papapetrou (MP) metric [14, 15], which is an exact solution of Einstein's equations that describes a static binary of extremally charged black holes. Despite its mathematical simplicity, the MP solution has recently been used as a surrogate model for black hole binaries in order to understand how single black hole phenomena transpose to a binary system. For instance, Ref. [16] has employed the MP metric to understand the connection between quasinormal modes and light rings in the context of black hole binaries. Refs. [17, 18], on the other hand, have computed the shadows cast by an MP binary to better understand chaotic scattering in a binary black hole system. The resulting shadow shares many similarities and qualitative features with the shadows computed in Ref. [19] using a numerically simulated binary

black hole background. Ref. [20] has also applied the MP metric to analyze particle scattering around a black hole binary and asserted its effectiveness in approximating a head on collision in the limit of large separations and small approach speeds. We followed an analog approach in order to gain physical intuition and qualitative insights about energy extraction from black hole binaries by the Penrose mechanism. In particular, we extended the concept of a particle dependent *generalized ergosphere* [21], which enables the extraction of electromagnetic energy from Reissner-Nördstrom (RN) black holes, to the MP solution and study how the energy extraction efficiency is affected by the presence of a companion black hole.

Taking into account the fact that, in astrophysical contexts, any excess of electric charge in a black hole tends to be quickly neutralized [22], we also considered rotating systems in our work. More specifically, in order to illustrate how the main results for the MP spacetime can be extrapolated to a binary system composed of Kerr black holes, we employ a static exact and analytic solution of Einstein's field equations, discovered independently by Cabrera-Munguia, Manko and Ruiz (hereby referred to as the CMMR metric) [23, 24, 25]. The CMMR metric describes two generic Kerr black holes that do not coalesce thanks to the presence of a "strut" that holds them apart at a fixed distance. In particular, we sketched the ergosphere of the CMMR spacetime for a selected set of parameters and gave an example of a Penrose process around a binary of rotating black holes.

The combined results presented in Sections 2.3 and 2.4 have been compiled in a paper and were published Ref. [26]. As an extension to this work, we have begun the development of a framework that should allow one to observe the PP for an arbitrary spacetime and shall present these preliminary results in Sec. 2.5. We illustrate the viability of our proposition by utilizing a non-exact solution to Einstein's field equations called the SKS solution, that models an orbiting binary of rotating black holes close to merger.

2.2 A brief review of the Penrose process in the Kerr spacetime

In this section, we shall briefly review energy extraction of rotating and charged black holes via the Penrose Process to familiarize the reader with the underlying physical concepts, methods and techniques involved in the mechanism. This is important since these tools will be necessary later on while we present novel results. Our review will follow closely Ref. [27]. We start by reminding that the Kerr metric, in Boyer-Lindquist coordinates (t, r, θ, ϕ) is given by

$$
\begin{aligned}
ds^2 = &-\left(1 - \frac{2Mr}{\rho^2}\right) dt^2 - \frac{2Mar\sin^2\theta}{\rho^2}(dtd\phi + d\phi dt) \\
&+ \frac{\rho^2}{\Delta}dr^2 + \rho^2 d\theta^2 + \frac{\sin^2\theta}{\rho^2}\left[(r^2 + a^2)^2 - a^2\Delta\sin^2\theta\right]d\phi^2,
\end{aligned} \quad (2.1)
$$

where

$$
\Delta(r) = r^2 - 2Mr + a^2 \tag{2.2}
$$

and

$$
\rho^2(r, \theta) = r^2 + a^2\cos^2\theta. \tag{2.3}
$$

The constants M, J and $a = J/M$ represent, respectively the black hole's mass, angular momentum and spin parameter. The metric possesses two event horizons, located at

$$
r_{H\pm} = M \pm \sqrt{M^2 - a^2} \tag{2.4}
$$

and since its components are independent of both the coordinate time t and the axial angular variable ϕ, there are global Killing vector fields $K = \partial_t$ and $R = \partial_\phi$ that generate these symmetries. Since the metric is stationary, the region where the time-like global Killing vector field changes its sign and thus static observers become prohibited does not coincide with the event horizons. In fact, one can easily see that

$$
K^\mu K_\mu = -\frac{1}{\rho^2}\left(\Delta - a^2\sin^2\theta\right) = -\frac{a^2 + r(r - 2M) - a^2\sin^2\theta}{(r^2 + a^2\cos^2\theta)^2}. \tag{2.5}
$$

and thus $K^\mu K_\mu = 0$ implies that the killing horizons are located at

$$r_{K\pm} = M \pm \sqrt{M^2 - a^2 \cos^2 \theta}. \tag{2.6}$$

which means that r_{K+} is outside r_{H+}, coinciding with it only at the poles ($\theta = 0$ or $\theta = \pi$). Notice also that using r_{H+} in Eq. (2.5) yields $\Delta = 0$ and thus

$$K^\mu K_\mu = \frac{a^2}{\rho^2} \sin^2 \theta \geq 0. \tag{2.7}$$

The region that lies in-between r_{K+} and r_{H+} is called the *ergosphere* or *ergoregion*. The fact that this region is outside the event horizons and that $K^\mu K_\mu > 0$ in it is paramount to the Penrose mechanism, as we shall see further on. A schematic representation of important structures in the Kerr spacetime can be found in Fig. 2.1, where the ergosphere is shaded in gray.
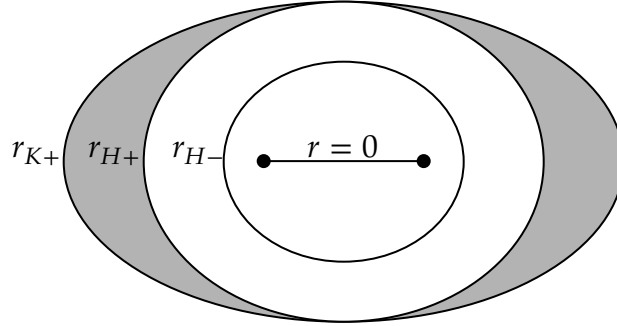
Figure 2.1: Schematic representation of important boundaries and regions in a Kerr black hole. The gray region represents the BH's ergosphere. The black hole's rotational axis goes across the figure, from bottom to top.

Let us now consider a particle of 4-momentum p^μ moving along a time-like geodesic in the Kerr spacetime parametrized by its proper time τ. The energy of the particle along its trajectory, as measured by a static observer infinitely far away from the black hole, is given by

$$E = -K_\mu p^\mu. \tag{2.8}$$

Outside the ergosphere, K^μ is time-like and $K_\mu p^\mu / < 0$. Since we would like

the energy to be positive infinitely far away from the BH, we must introduce a leading minus sign in Eq. (2.8). On the other hand, inside the ergosphere K^μ is space-like and $K_\mu p^\mu / > 0$ which implies that in this region $E < 0$. It is important to remark that, despite the energy being negative relatively to a static observer at infinity, it still remains positive according to a local observer. Furthermore, it can be shown that these negative energy orbits must be confined within the ergosphere and must always cross the outer horizon [28, 29], so there is no risk of such negative energy particles "leaking out" to infinity.

Let us now imagine that a particle labeled as (0) traveling in the Kerr spacetime comes from infinity with 4-momentum $p^{(0)\mu}$ and decays *inside* the ergosphere in a break-up point b into two other particles, the first of which labeled (1) has 4-momentum $p^{(1)\mu}$ and gets absorbed by the black hole and the second of which labeled (2), 4-momentum $p^{(2)\mu}$ and escapes the gravitational pull of the system and returns to infinity. The law of conservation of 4-momentum applied at point b implies that

$$p^{(0)\mu} = p^{(1)\mu} + p^{(2)\mu}. \tag{2.9}$$

Contracting Eq. (2.9) with K^μ we get

$$E^{(0)} = E^{(1)} + E^{(2)}. \tag{2.10}$$

If we engineer the trajectory of particle (1) such that $E^{(1)} < 0$, we get

$$E^{(2)} = E^{(0)} + E^{(1)} > E^{(0)}, \tag{2.11}$$

which means that the energy of the returning particle is greater than the energy of the original. This mechanism is precisely the one proposed by Penrose and Floyd, and has since been known since as the *Penrose Process* or *Penrose Mechanism*. This break-up process is represented in Fig. 2.2.

Where does the excess energy of particle (2) comes from? To answer that, let us analyze particle (1) as it crosses the outer horizon. In the Kerr metric, the event horizons are Killing horizons of the Killing vector formed by a linear
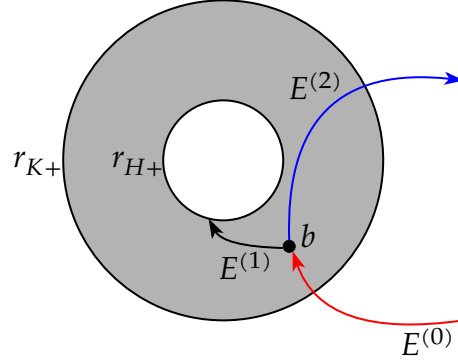
Figure 2.2: Schematic representation of a Penrose process. A particle of energy $E^{(0)}$ (red) comes in from infinity and decays at point b inside the ergosphere in a negative energy $E^{(1)}$ trajectory (black) and a positive energy $E^{(2)} > E^{(0)}$ trajectory (blue) that returns to infinity. The black hole's rotational axis is pointing outside the page, towards the reader.

combination of the two spacetime symmetries, namely

$$\chi^{\mu} = K^{\mu} + \Omega R^{\mu} \tag{2.12}$$

where Ω is the horizon's angular velocity. Considering that particle (1) crosses the event horizon while remaining time-like and χ^{μ} is null at the outer horizon, we must have that

$$p^{(1)\mu}\chi_{\mu} = -E^{(1)} + \Omega L^{(1)} < 0 \tag{2.13}$$

where $L^{(1)}$ represents the particle's angular momentum. In order to satisfy Eq. (2.13) given that $E^{(1)} < 0$ and $\Omega > 0$ we must have that

$$L^{(1)} < \frac{E^{(1)}}{\Omega}, \tag{2.14}$$

which implies that $L^{(1)} < 0$ and thus the negative energy particle must be rotating in the opposite direction of the black hole. This means that when the negative energy particle gets absorbed, the BH looses a small amount of its own angular momentum, transferring it to the particle that is to be ejected back to infinity.

Naturally at this point one may start to wander if it is possible to completely

"drain" the black hole via repeated Penrose processes. Christodoulou in Ref. [30] has determined that there is a limit of energy extraction, expressed by an *irreducible mass*, that is, a lower mass bound for the black hole to achieve from which no further energy can be extracted. To see that, let us consider that when particle (1) interacts with the BH, energy is conserved and thus the loss in mass and angular momentum of the black hole corresponds respectively to $E^{(1)}$ and $L^{(1)}$, that is,

$$dM = E^{(1)}, \tag{2.15}$$

$$dJ = L^{(1)}. \tag{2.16}$$

By virtue of Eq. (2.14), we get that

$$dJ < \frac{dM}{\Omega}. \tag{2.17}$$

The maximum energy extraction occurs when we exactly reach this limit. Given that

$$\Omega = \frac{a}{r_{H+}^2 + a^2} \tag{2.18}$$

we can solve

$$\frac{dM}{dJ} = \frac{a}{r_{H+}^2 + a^2} \tag{2.19}$$

for $M(J)$ with $M(0) = M_0$ to find

$$M_0^2 = \frac{1}{2} \left(M^2 + \sqrt{M^4 - J^2} \right), \tag{2.20}$$

which is known as the *irreducible mass*. To see why that is the case, one can take the differential of Eq. (2.20) to find

$$dM_0 = \frac{a}{4M_0 \sqrt{M^2 - a^2}} \left(\Omega^{-1} dM - dJ \right). \tag{2.21}$$

Thanks to Eq. (2.17), we can infer from Eq. (2.21) that $dM_0 > 0$ always, thus M_0 cannot be reduced (hence it's name) and gives the lower energy bound that the black hole can achieve. The formula for the maximum energy that can be

21

extracted is thus

$$M - M_0 = M - \frac{1}{\sqrt{2}} \left(M^2 + \sqrt{M^4 - J^2} \right)^{1/2}. \tag{2.22}$$

By considering an extreme BH (with $a = 1$), Eq. (2.22) states that approximately 29% of the BH's energy can be extracted via the Penrose process. One can get to the same conclusion by starting of with Hawking's area theorem, which states that the event horizon area cannot decrease (See Ref. [27] page 270).

2.3 Majumdar-Papapetrou Spacetime

The Majumdar-Papapetrou (MP) spacetime is a static electrovacuum solution of Einstein's equations that represents a set of extremal black holes whose mutual gravitational attraction is cancelled by their mutual electromagnetic repulsion [14, 15, 31]. For two black holes of masses M_1 and M_2 and electric charges $Q_1 = M_1$ and $Q_2 = M_2$, in equilibrium and separated by a distance $2a$ along the z-axis, the MP line element, in Weyl's cylindrical coordinates (t, ρ, ϕ, z), is given by [32]

$$ds^2 = -\frac{dt^2}{U(\rho, z)^2} + U(\rho, z)^2 \left[d\rho^2 + \rho^2 d\phi^2 + dz^2 \right], \tag{2.23}$$

where

$$U(\rho, z) = 1 + \frac{M_1}{\sqrt{\rho^2 + (z + a)^2}} + \frac{M_2}{\sqrt{\rho^2 + (z - a)^2}}. \tag{2.24}$$

The electromagnetic potential A_μ associated with the MP solution is

$$A_\mu = \left(1 - \frac{1}{U} \right) \delta_{\mu t}, \tag{2.25}$$

where $\delta_{\mu\nu}$ is the Kronecker delta. We note that Weyl's coordinates describe only the exterior of the black holes. The event horizons and the black holes themselves are collapsed into the points $\rho = 0$, $z = \pm a$. We denote the total mass of the binary system by $M_T = M_1 + M_2$ and its mass ratio by $M_R = M_2/M_1$.

Without loss of generality, we assume that $0 \leq M_R \leq 1$.

Being described by a static metric, the MP spacetime does not possess an ergosphere in the sense described in Sec. 2.2. Consequently, the energy associated with geodesic motion in the MP spacetime is always positive, meaning that energy extraction by free particles is impossible. Charged particles, however, interact with charged black holes through Lorentz forces and, hence, do not follow geodesics. If the electromagnetic interaction is attractive, negative energy trajectories and energy extraction are, in principle, possible. For a single charged black hole described by the RN metric, the fact that the Penrose process is viable was shown in Ref. [33]. Building on the notion of a generalized ergosphere [21, 33], we shall study the motion of charged particles around the MP spacetime to investigate the possibility of negative energy motion and energy extraction.

2.3.1 Motion of charged particles in MP

The motion of a massive charged test particle (with charge-to-mass ratio μ) in a spacetime with metric $g_{\mu\nu}$, subject to the electromagnetic potential A_μ, is determined by the Lagrangian

$$\mathcal{L} = \frac{1}{2} g_{\mu\nu} \dot{x}^\mu \dot{x}^\nu - \mu A_\alpha \dot{x}^\alpha, \tag{2.26}$$

where $x^\mu = x^\mu(\lambda)$ denotes the position of the particle at proper time λ and the dots represent derivatives with respect to λ. Adopting Weyl's cylindrical coordinates, and taking into account the explicit form of the MP metric, the Lagrangian above can be recast as [34]

$$\mathcal{L} = \frac{1}{2} \left[-\frac{\dot{t}^2}{U^2} + U^2 \left(\dot{\rho}^2 + \rho^2 \dot{\phi}^2 + \dot{z}^2 \right) \right] - \mu \left(1 - \frac{1}{U} \right) \dot{t}. \tag{2.27}$$

Since the Lagrangian does not depend explicitly on t and ϕ, two constants of motion (as measured by freely-falling observers at infinity) can be readily identified. The constant associated with the time symmetry is the energy

divided by the mass m of the particle:

$$E = -\frac{\partial \mathcal{L}}{\partial \dot{t}} = \frac{\dot{t}}{U^2} + \mu \left(1 - \frac{1}{U} \right). \tag{2.28}$$

The constant associated with the angular symmetry is the angular momentum per unit mass (with respect to the z axis):

$$L = \frac{\partial \mathcal{L}}{\partial \dot{\phi}} = U^2 \rho^2 \dot{\phi}. \tag{2.29}$$

Given that the particle is following a time-like trajectory, it's 4-velocity is subjected to the normalization condition

$$g_{\mu\nu} \dot{x}^\mu \dot{x}^\nu = -\frac{\dot{t}^2}{U^2} + U^2 \left(\dot{\rho}^2 + \rho^2 \dot{\phi}^2 + \dot{z}^2 \right) = -1. \tag{2.30}$$

Solving Eq. (2.28) for $\dot{t}$ and Eq. (2.29) $\dot{\phi}$ and substituting the results back into Eq. (2.30), we obtain a quadratic equation for E, which in turn can be solved to yield

$$E = \mu \left(1 - \frac{1}{U} \right) + \sqrt{\frac{L^2}{\rho^2 U^4} + \frac{1}{U^2} + \dot{\rho}^2 + \dot{z}^2}, \tag{2.31}$$

where the negative root has been ignored due to the fact that E must be positive for particles at infinity when $\mu = 0$ (see Ref. [21] for a detailed discussion about positive and negative root states for E). We note that Eq. (2.31) reduces to the expression found in Ref. [33] for a RN black hole if the mass of one of the black holes is taken to be zero and an appropriate coordinate system, centered around the other black hole, is adopted. For convenience and later use, we rewrite Eq. (2.31) as

$$\dot{\rho}^2 + \dot{z}^2 = E_{\text{eff}}^2(\rho, z) - V_{\text{eff}}(\rho, z), \tag{2.32}$$

where

$$E_{\text{eff}}(\rho, z) = E - \mu \left(1 - \frac{1}{U} \right), \tag{2.33}$$

and

$$V_{\text{eff}}(\rho, z) = \frac{L^2}{\rho^2 U^4} + \frac{1}{U^2}. \tag{2.34}$$

Note that the quantities defined above are subject to the following constraints:

$$E_{\text{eff}}(\rho, z) \geq 0, \qquad E_{\text{eff}}^2(\rho, z) \geq V_{\text{eff}}(\rho, z). \tag{2.35}$$

The equations of motion are obtained directly from the Euler-Lagrange equations. After using Eqs. (2.28) and (2.29) to eliminate $\dot{t}$ and $\dot{\phi}$, one is left with

$$\ddot{\rho} - \frac{L^2(U + \rho \partial_\rho U)}{\rho^3 U^5} + \frac{2\dot{\rho}\dot{z}\partial_z U - (E^2 + \dot{z}^2 - \dot{\rho}^2)\partial_\rho U}{U}$$
$$- \frac{\mu}{U}\left(\mu - 2E + \frac{E - \mu}{U}\right)\partial_\rho U = 0, \tag{2.36}$$

and

$$\ddot{z} - \frac{L^2 \partial_z U}{\rho^2 U^5} + \frac{2\dot{\rho}\dot{z}\partial_\rho U - (E^2 - \dot{z}^2 + \dot{\rho}^2)\partial_z U}{U}$$
$$- \frac{\mu}{U}\left(\mu - 2E + \frac{E - \mu}{U}\right)\partial_z U = 0, \tag{2.37}$$

which reduce to the equations of motion found in Ref. [16] for neutral particles. Together with Eqs. (2.28) and (2.29), the two equations above fully determine the trajectory of a massive charged particle in the MP spacetime once appropriate initial conditions have been specified. In fact, we first specify the energy E, the angular momentum L, and the initial values for ρ, z, and $\dot{z}$. The initial value for $\dot{\rho}$ is determined from Eq. (2.31). Using this information, we can solve the system of equations (2.36)-(2.37) to obtain $\rho(\lambda)$ and $z(\lambda)$. The final step is the integration of Eqs. (2.28) and (2.29), subject to the initial data for t and ϕ, to find $t(\lambda)$ and $\phi(\lambda)$.

2.3.2 Generalized Ergosphere

We want to know if charged particles can have negative energies in the MP spacetime. From Eq. (2.31) it is evident that, for fixed μ, the energy is completely determined by the angular momentum L, and the values of ρ, z, $\dot{\rho}$ and $\dot{z}$ at any given instant of time. At a fixed position, the minimum possible energy

is associated with particles at rest. Letting $\dot{\rho} = \dot{z} = 0$ and $L = 0$ (i.e. $\dot{\phi} = 0$), we conclude that the minimum energy (per unit mass) allowed for a particle sitting at (t, ρ, ϕ, z) is

$$E_{\min} = \mu \left(1 - \frac{1}{U} \right) + \frac{1}{U}. \tag{2.38}$$

This minimum energy will be negative if the following two conditions are satisfied: Since $U \geq 1$, μ must be negative, meaning that the charge of the particle must be opposite to the charge of the black holes. Additionally, the resting particle must be inside the spatial region determined by

$$\frac{1}{\sqrt{\bar{\rho}^2 + (\bar{z} + 1)^2}} + \frac{M_R}{\sqrt{\bar{\rho}^2 + (\bar{z} - 1)^2}} > -\frac{1 + M_R}{\bar{\mu}}, \tag{2.39}$$

where $\bar{\rho} = \rho/a$, $\bar{z} = z/a$ and $\bar{\mu} = \mu M_T/a$ are dimensionless quantities. The parameter $\bar{\mu}$ can be understood as a measure of the potential energy (per unit particle mass) associated with the electromagnetic interaction between the particle and the binary. The inequality above determines the generalized ergosphere of the MP spacetime: particles with opposite charge in relation to the black hole and located inside the region determined by Eq. (2.39) will have negative energies if their velocities are sufficiently small. Particles outside, on the other hand, will have positive energies regardless of their velocities.

Note that the notion of a generalized ergosphere depends not only on the geometry of the spacetime, but also on properties of the particle (through the charge-to-mass ratio μ), as in Refs. [21, 33]. In particular, the shape of the ergosphere depends only on the parameters M_R and $\bar{\mu}$. In order to understand this dependence, we plot the generalized ergosphere for nine M_R-$\bar{\mu}$ pairs. Each pair corresponds to a point in the parameter space of Fig. 2.3 and is labeled by a letter (**A-I**). The $\phi = 0$ section of the associated ergospheres are shown in Fig. 2.4. Due to the axial symmetry of the problem, the ergospheres are the solids of revolution obtained by the rotation of the regions shown in Fig. 2.4 with respect to the $\bar{z}$-axis. Note that the generalized ergosphere can be either a single connected region (for parameters inside the red section of Fig. 2.3) or the disjoint union of two connected regions[1] (for parameters in the green section of

---

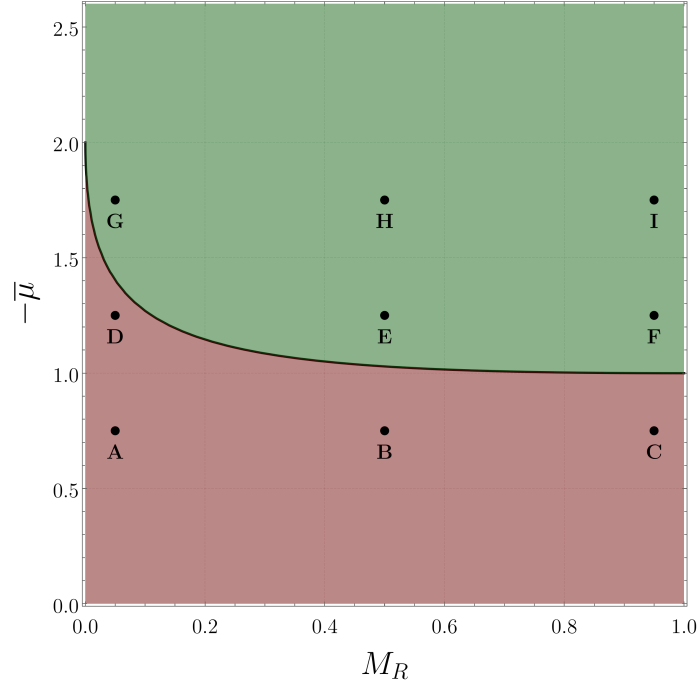[1]In such a case we shall refer to each connected region as a single ergosphere.

Figure 2.3: The parameter space M_R-$\overline{\mu}$. The generalized ergosphere exists if and only if $\overline{\mu} < 0$. It consists of a single connected region for any point inside the red section. For points in the green section, on the other hand, the ergosphere is the disjoint union of two connected regions. The black curve marks the boundary between connected and disconnected ergospheres. The ergospheres associated with the black labeled dots are plotted in Fig. 2.4.

Fig. 2.3). The boundary separating connected and disconnected ergospheres, represented by the black line in Fig. 2.3, corresponds to the saturation of Eq (2.39).

The ergosphere becomes more evenly distributed around the black holes when the mass ratio M_R approaches one. This is seen in Fig. 2.3 by following the points $\mathbf{A} \rightarrow \mathbf{B} \rightarrow \mathbf{C}$, or $\mathbf{D} \rightarrow \mathbf{E} \rightarrow \mathbf{F}$, or $\mathbf{G} \rightarrow \mathbf{H} \rightarrow \mathbf{I}$. Furthermore, if $-2 < \overline{\mu} < -1$, we see that an increase in the mass ratio may produce a single ergosphere from two disjoint ones, as in $\mathbf{D} \rightarrow \mathbf{E}$. Similarly, for any mass ratio, an increase in the absolute value of $\overline{\mu}$ can also induce the merger of the ergospheres, as in $\mathbf{D} \rightarrow \mathbf{G}$, $\mathbf{B} \rightarrow \mathbf{E}$ and $\mathbf{C} \rightarrow \mathbf{F}$. In fact, no matter what the mass ratio is, if $-\overline{\mu}$ is sufficiently small, each black hole will be surrounded by its own ergosphere. In contrast, if $-\overline{\mu}$ is sufficiently large, there will be a single ergosphere surrounding
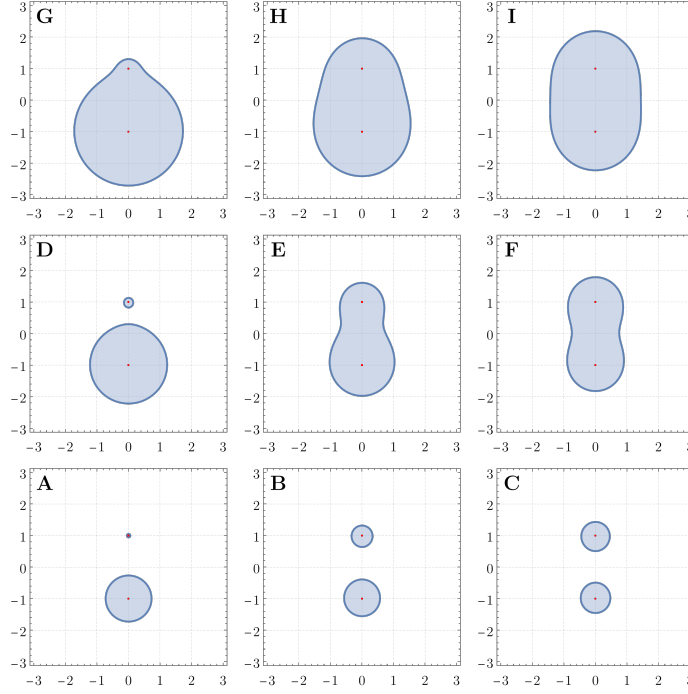
Figure 2.4: The $\phi = 0$ section of the ergosphere for different points (labeled **A-I**) in the parameter space of Fig. 2.3. In each plot the horizontal and vertical axes are $\bar{\rho}$ and $\bar{z}$, respectively. The red dots indicate the location of the black holes.

the binary black hole. Finally, we remark that, according to Eq. (2.39), the effects of the charge of the particle, of the total mass of the binary and of the separation parameter are all combined in $\bar{\mu}$. Therefore, as far as the visualization of the ergosphere is concerned, the effect of increasing $|\mu|$ is exactly the same as increasing M_T or decreasing a.

The minimum energy (per unit mass) at a given point of the spacetime, in contrast, depends on the explicit values of μ, M_R and M_T/a. To illustrate this dependence, we plot in Fig. 2.5 the energy levels inside the ergosphere determined by $M_R = 1/2$ and $\bar{\mu} = -5/4$ (which corresponds to the point **E** in Figs. 2.3 and 2.4) for different combinations of μ and M_T/a. The color bar in Fig. 2.5 indicates the value of $E_{\min}/\mu$, which, according to Eq. (2.38), varies from zero (at the boundary of the ergosphere) to one (at the black holes). As $|\mu|$ decreases and M_T/a increases (while $\bar{\mu}$ and M_R are kept fixed), the shape of the ergosphere remains unchanged, but the energy levels become more evenly
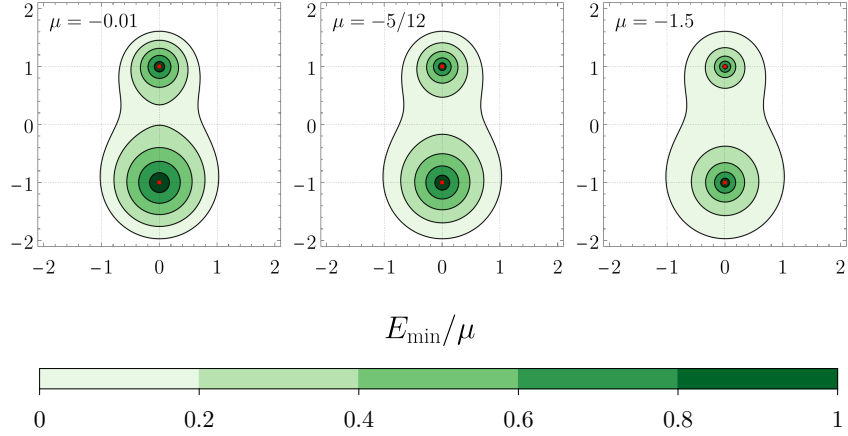
Figure 2.5: Energy levels inside the generalized ergosphere of a MP black hole with $M_R = 1/2$ and $\overline{\mu} = -5/4$, corresponding to the point **E** in Figs. 2.3 and 2.4. The color bar represents $E_{\min}/\mu$. From left to right, the panels correspond respectively to $\mu = -0.01$, $\mu = -5/12$, and $\mu = -1.5$. The horizontal and vertical axes in each panel are $\overline{\rho}$ and $\overline{z}$, respectively. The red dots indicate the location of the black holes.

distributed around the black holes.

2.3.3 Negative energy trajectories

Trajectories associated with negative energies are confined within the ergosphere defined by Eq. (2.39). For a generic set of initial conditions, such paths will eventually end up at either one of the black holes. This is not much different from the case of a single RN or a Kerr black hole, in which particles with negative energies that start outside the event horizon necessarily enter the black hole and reach the spacetime singularity. Instead of focusing on this type of trajectory, we concentrated on trajectories which have no analogs in standard (Kerr and RN) black hole spacetimes [28, 35]. We want to investigate whether closed orbits of negative energy that live outside the black holes are allowed. It's important to first note, however, that if the Kerr black hole is immersed in an external magnetic field, closed orbits of negative energy are allowed outside the event horizon [36, 37]. We also note that stable circular orbits of negative energy exist around a Kerr naked singularity (and that the Penrose process

can effectively take place using such orbits) [38]. We follow the procedure described in the last paragraph of section 2.3.1 to solve the equations of motion. To simplify our work, we restrict our attention to two classes of planar motion and show that, by fine-tuning the initial data, one is able to find closed orbits of negative energies in the MP spacetime. These closed orbits of negative energies are unstable, in the sense that generic perturbations of the initial conditions result in trajectories that end at one of the black holes.

The first class of orbits assumes zero angular momentum ($L = 0$) so that the trajectories are restricted to a plane that contains both black holes (here we choose the $\phi = 0$ plane without loss of generality). For a given set of parameters $a, M_1, M_2, E,$ and μ, after fixing $\rho(0) = 0$ and $\dot{z}(0) = 0$, we fine tune the initial position $z(0)$. The initial value $\dot{\rho}(0)$ is determined from Eq. (2.31). To illustrate, we show in Fig. 2.6 two examples of eight-shaped orbits obtained with this scheme. The left panel of Fig. 2.6 represents an orbit with energy (per unit mass) $E = -2/10$ and charge-to-mass ratio $\mu = -5$ for an equal mass MP binary ($M_1 = M_2 = 1$) with separation parameter $a = 1$. The trajectory starts on the z-axis, at $z(0) = 5.314064237978...$ (fine-tuned). One complete revolution of the trajectory, with corresponding period of $\lambda \approx 22.64$, is shown. The right panel of Fig. 2.6, on the other hand, exhibits an orbit of $E = -2/10$ and $\mu = -5$ for a MP binary with mass ratio $M_R = 1/2$ ($M_1 = 2, M_2 = 1$) and separation parameter $a = 1$. The trajectory starts on the z-axis, at $z(0) = 12.832155724084...$ (fine-tuned). One complete revolution of the trajectory, with corresponding period of approximately $\lambda \approx 43.28$, is shown.

The second class of orbits is only possible for equal mass binaries and comprises trajectories that are confined to the $z = 0$ plane, which is the plane equidistant to the black holes. Particles with negative energy whose motion is constrained to this plane will evolve in a perpetual oscillatory motion, either in straight lines (when $L = 0$) or in more complicated precessing orbits (when $L \neq 0$). Even though these trajectories are unstable to generic perturbations, on the plane itself they are stable. In other words, infinitesimal perturbations of $\rho(0)$ and $\dot{\rho}(0)$ produce infinitesimal variations on the original trajectory (if $z(0)$ and $\dot{z}(0)$ are kept fixed).

To analyze these orbits we resort to Eqs. (2.32)-(2.34). Given a, E and L, the
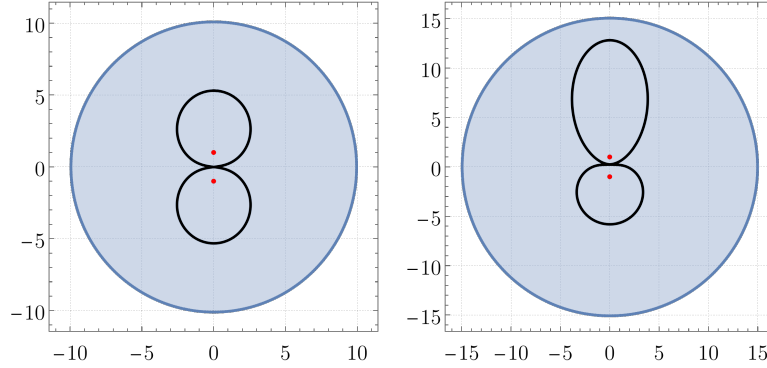
Figure 2.6: Example of closed trajectories of negative energy (black curves) in the plane containing the black holes. The blue region is the generalized ergosphere of the spacetime, while the red dots indicate the location of the black holes. The horizontal and vertical axes in each panel are $\bar{\rho}$ and $\bar{z}$, respectively. Left panel: trajectory corresponding to $L = 0$, $E = -2/10$, $a = M_1 = M_2 = 1$, $\mu = -5$, $\rho(0) = 0$, $z(0) = 5.314064237978...$ (fine-tuned), and $\dot{z}(0) = 0$. The associated period of revolution is $\lambda \approx 22.64$. Right panel: trajectory corresponding to $L = 0$, $E = -2/100$, $a = 1$, $M_1 = 2M_2 = 2$, $\mu = -5$, $\rho(0) = 0$, $z(0) = 12.832155724084...$ (fine-tuned), and $\dot{z}(0) = 0$. The associated period of revolution is $\lambda \approx 43.28$.

critical points ρ where $E_{\mathrm{eff}}(\rho, 0)^2 = V_{\mathrm{eff}}(\rho, 0)$ represent circular closed orbits. Typically, however, the particle will be confined inside a compact section of the $z = 0$ plane, in a characteristic "zoom-whirl" orbit [16, 39], moving between a minimum radius ρ_{min} and a maximum radius ρ_{max}. In Fig. 2.7, we show the effective energy and the effective potential for a MP spacetime with $a = 1$ and $M_1 = M_2 = 1$, when the particle's charge-to-mass ratio, angular momentum (per unit mass), and energy (per unit mass) are, respectively, $\mu = -5$, $L = 12.85869$, and $E = -5/100$. The particle is constrained to move between $\rho_{\mathrm{min}} \approx 0.543$ and $\rho_{\mathrm{max}} \approx 3.857$. The corresponding trajectory, assuming the starting point to be $\rho(0) = 2$ and $\phi(0) = 0$, is also shown in Fig. 2.7.

2.3.4 Penrose Process

Following Penrose's original proposal [8] and its extension to RN black holes [21, 33], we now investigate the possibility of energy extraction from a
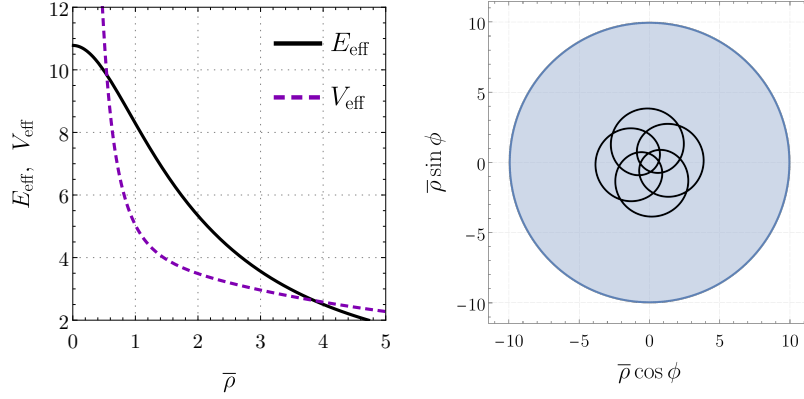
Figure 2.7: Left panel: effective energy (black curve) and effective potential (purple dashed curve) for $L = 12.85869$, $E = -5/100$, $a = 1$, $M_1 = M_2 = 1$, $\mu = -5$. Right panel: an example of a closed trajectory of negative energy in the $z = 0$ symmetry plane. The blue region is the generalized ergosphere of the spacetime. The trajectory (black curve) is generated by setting the parameters to $L = 12.85869$, $E = -5/100$, $a = 1$, $M_1 = M_2 = 1$, $\mu = -5$, $\rho(0) = 2$, and $\phi(0) = 0$. The associated period of revolution is $\lambda \approx 35$.

MP binary black hole. The mechanism we shall explore is analogous to the most standard one: a negatively charged particle is sent towards the binary black hole and, once inside the generalized ergosphere, breaks up into two fragments, one of which escapes to infinity with more energy than the original particle. We assume that the incident particle follows a trajectory $T_{(0)}$, which starts outside the ergosphere and ends inside it, at the break-up point (ρ_*, ϕ_*, z_*). From the break-up point, two other trajectories, labeled $T_{(1)}$ and $T_{(2)}$, start. Each trajectory $T_{(i)}$ is a time-like path $x^\mu_{(i)}(\lambda)$ parametrized by its proper time λ. To fix notation, let $m_{(i)}$, $\mu_{(i)}$, $E_{(i)}$, $L_{(i)}$, and $P^\mu_{(i)}$ denote, respectively, the mass, the charge-to-mass ratio, the energy per unit mass, the angular momentum per unit mass (with respect to the z-axis), and the 4-momentum of the particle i on trajectory $T_{(i)}$. We assume that fragment 1 remains inside the ergosphere (meaning that $E_{(1)} < 0$), while fragment 2 escapes back to infinity.

The quantities that characterize each particle are related by conservation equations. Charge conservation, for instance, yields

$$\mu_{(0)} m_{(0)} = \mu_{(1)} m_{(1)} + \mu_{(2)} m_{(2)}. \tag{2.40}$$

The conservation of the four-momentum applied at the break-up point, on the other hand, reads

$$P^{\mu}_{(0)} = P^{\mu}_{(1)} + P^{\mu}_{(2)}. \tag{2.41}$$

Each component of the vector equation (2.41) above corresponds to a different conservation equation with straightforward physical interpretation. The zero-component is just the conservation of total energy, i.e.

$$E_{(0)}m_{(0)} = E_{(1)}m_{(1)} + E_{(2)}m_{(2)}. \tag{2.42}$$

The spatial components are the conservation of linear momenta, i.e.

$$\begin{cases} m_{(0)}\dot{\rho}_{(0)} = m_{(1)}\dot{\rho}_{(1)} + m_{(2)}\dot{\rho}_{(2)} \\ m_{(0)}\dot{z}_{(0)} = m_{(1)}\dot{z}_{(1)} + m_{(2)}\dot{z}_{(2)} \end{cases}, \tag{2.43}$$

and the conservation of angular momentum, i.e.

$$L_{(0)}m_{(0)} = L_{(1)}m_{(1)} + L_{(2)}m_{(2)}. \tag{2.44}$$

We remark that all derivatives in (2.43) are evaluated at the break-up point. We also note that the break-up of the incident particle naturally imposes restrictions on the masses of its fragments. By squaring Eq. (2.41) and using the fact that the four-momentum is future-pointing and time-like, we obtain the inequality [40]

$$m^2_{(1)} + m^2_{(2)} < m^2_{(0)}. \tag{2.45}$$

i	$m_{(i)}$	$\mu_{(i)}$	$E_{(i)}$	$L_{(i)}$	$\dot{\rho}_{(i)}$	$\dot{z}_{(i)}$
0	1.00000	-0.08345	1.00000	0	0.60000	0.09699
1	0.70000	-5.00000	-0.02000	0	0.41207	0.00000
2	0.23248	14.69629	4.36171	0	1.34012	0.41719

Table 2.1: Parameters that generate the trajectories $T_{(0)}$, $T_{(1)}$, and $T_{(2)}$ of the Penrose process shown in the left panel of Fig. 2.8. The derivatives $\dot{\rho}_{(i)}$ and $\dot{z}_{(i)}$ are evaluated at the break-up point.

From Eq. (2.42), the energy carried away by the escaping fragment is
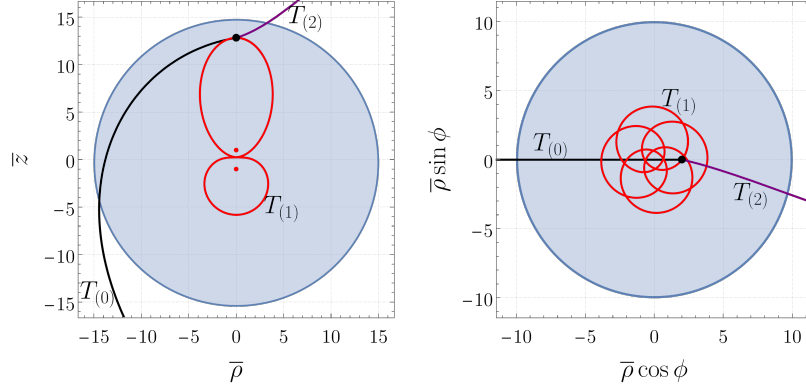
Figure 2.8: Left panel: Penrose process in the ρ-z plane of a MP spacetime with $M_1 = 2$, $M_2 = 1$, and $a = 1$. Right panel: Penrose process in the $z = 0$ plane of a MP spacetime with $M_1 = M_2 = 1$ and $a = 1$. In each plot, the incoming trajectory $T_{(0)}$ (black curve) splits at the black point into the negative energy orbit $T_{(1)}$ (red curve) and the trajectory of the escaping fragment $T_{(2)}$ (purple curve). The parameters that generate these trajectories are shown in Tables 2.1 and 2.2. The blue region is the generalized ergosphere (for particle 1) and the red dots indicate the location of the black holes.

$E_{(2)}m_{(2)} = E_{(0)}m_{(0)} - E_{(1)}m_{(1)}$. Since we have assumed that $E_{(1)} < 0$, the escaping particle will carry away more energy than the incident particle had. If the negative energy fragment collapses to one of the black holes, it will directly decrease the energy associated with the black hole, as in Penrose's original proposal. If, on the other hand, the negative energy fragment remains in a closed orbit (such as the ones described in Sec. 2.3.3), where does the extra energy for the escaping fragment come from? Since the final state (binary black hole and bound particle fragment) is less energetic than the binary itself, we conclude that the extracted energy is associated with the binding energy of the binary. In other words, the presence of the bound particle fragment reduces the energy required to form a MP binary and the excess energy is transferred to the escaping fragment.

In Fig. 2.8 we exhibit examples of Penrose processes that include some of the negative energy orbits shown in Sec. 2.3.3. The left panel exhibits a Penrose process that takes place in the ρ-z plane of a MP spacetime with $M_1 = 2$, $M_2 = 1$, and $a = 1$. The incoming particle breaks-up at $\bar{\rho} = 0$ and $\bar{z} = 5.314064237978...$

i	$m_{(i)}$	$\mu_{(i)}$	$E_{(i)}$	$L_{(i)}$	$\dot{\rho}_{(i)}$	$\dot{z}_{(i)}$
0	1.00000	-0.27698	1.00000	0.00000	1.00000	0
1	0.10000	-5.00000	-0.05000	12.85870	1.36059	0
2	0.33342	0.66890	3.01423	-3.85662	2.59116	0

Table 2.2: Parameters that generate the trajectories $T_{(0)}$, $T_{(1)}$, and $T_{(2)}$ of the Penrose process shown in the right panel of Fig. 2.8. The derivatives $\dot{\rho}_{(i)}$ and $\dot{z}_{(i)}$ are evaluated at the break-up point.

(fine-tuned). The right panel, on the other hand, exhibits a Penrose process that occurs in the $z = 0$ plane of a MP spacetime with $M_1 = M_2 = 1$ and $a = 1$. The incoming particle breaks-up at $\bar{\rho} = 2$ and $\phi = 0$. The parameters that generate these examples and satisfy Eqs. (2.40)-(2.45) are given in Tables 2.1 and 2.2.

2.3.5 Energy extraction efficiency

The efficiency η of the Penrose process can be defined as the ratio between the energy output and the energy input. Using Eq. (2.42), we have

$$\eta = \frac{E_{(2)}m_{(2)} - E_{(0)}m_{(0)}}{E_{(0)}m_{(0)}} = -\frac{E_{(1)}m_{(1)}}{E_{(0)}m_{(0)}}. \tag{2.46}$$

A natural question arises: what is the maximum efficiency of the Penrose process in a MP spacetime? Since η is directly proportional to $E_{(1)}$ and inversely proportional to $E_{(0)}$, in order to maximize the efficiency of the process we need to make the absolute value of $E_{(1)}$ as large as possible and $E_{(0)}$ as small as possible. We also want the negative energy fragment to be as massive as possible in comparison to the mass of the incident particle. In other words, we want to extract as much energy as possible starting with as little energy as possible. We shall assume that the MP spacetime is fixed (meaning that M_1, M_2 and a are known), the break-up point has been specified as (ρ_*, z_*, ϕ_*) and the charge-to-mass ratio $\mu_{(1)}$ is known. Given these hypotheses, we will determine how much energy can be extracted from a MP black hole and how the remaining parameters must be chosen in order to optimize the process.

First, the minimum energy for an incident particle coming from infinity,

according to Eq. (2.31), is $E_{(0)} = 1$ and corresponds to the particle having zero kinetic energy at infinity. For that reason, we shall assume from now on that $L_{(0)} = 0$ and $E_{(0)} = 1$. Secondly, according to Eq. (2.38) and the discussion in the first paragraph of Sec. 2.3.2, the energy per unit mass of particle 1 is most negative if the particle is initially at rest. Therefore, at the break-up point we set

$$\dot{\rho}_{(1)} = \dot{z}_{(1)} = \dot{\phi}_{(1)} = 0, \tag{2.47}$$

meaning that the associated angular momentum per unit mass and energy per unit mass are, respectively, $L_{(1)} = 0$ and

$$E_{(1)} = E_{(1)}^{\min} = \mu_{(1)} \left(1 - \frac{1}{U_*} \right) + \frac{1}{U_*}, \tag{2.48}$$

where we have defined $U_* = U(\rho_*, z_*)$ for simplicity.

Let us now study the allowed values for $m_{(1)}$. The conservation of linear momenta, Eq. (2.43), yields the relation

$$m_{(2)}^2 = m_{(0)}^2 \left(\frac{\dot{\rho}_{(0)}^2 + \dot{z}_{(0)}^2}{\dot{\rho}_{(2)}^2 + \dot{z}_{(2)}^2} \right) + m_{(1)}^2 \left(\frac{\dot{\rho}_{(1)}^2 + \dot{z}_{(1)}^2}{\dot{\rho}_{(2)}^2 + \dot{z}_{(2)}^2} \right), \tag{2.49}$$

where all derivatives are evaluated at the break-up point. After replacing $\dot{\rho}_{(i)}^2 + \dot{z}_{(i)}^2$ using Eqs. (2.32)-(2.34), and employing the conservation equations (2.40), (2.42) and (2.44), the expression above reduces to

$$m_{(2)} = \sqrt{m_{(0)}^2 - 2m_{(0)} m_{(1)} \alpha_{(0)} + m_{(1)}^2}, \tag{2.50}$$

where

$$\alpha_{(0)} = U_* \left[1 - \mu_{(0)} \left(1 - \frac{1}{U_*} \right) \right]. \tag{2.51}$$

Note that the expression between brackets in the definition of $\alpha_{(0)}$ is precisely the effective energy of the incident particle evaluated at the break-up point as given by Eq. (2.33). The inequalities given in Eq. (2.35), together with the fact that $U_* \geq 1$, therefore imply that

$$\alpha_{(0)} \geq 1, \tag{2.52}$$

and

$$\mu_{(0)} \leq 1. \tag{2.53}$$

Eq. (2.50) and the fact that the masses are positive, together with the constraint imposed by Eq. (2.45), also imply that

$$0 < \frac{m_{(1)}}{m_{(0)}} < \alpha_{(0)}. \tag{2.54}$$

Since the radicand in Eq. (2.50) must be positive, the bound given by Eq. (2.54) can be further refined to yield

$$0 < m_{(1)} < m_{(0)} \left(\alpha_{(0)} - \sqrt{\alpha_{(0)}^2 - 1} \right). \tag{2.55}$$

Hence, the allowed range for $m_{(1)}$ is maximized when the inequalities (2.52) and (2.53) are saturated. In fact, when $\mu_{(0)} \to 1$ one can choose $m_{(1)} \to m_{(0)}$, thus maximizing the ratio $m_{(1)}/m_{(0)}$ that appears in Eq. (2.46). Consequently, the efficiency of the Penrose process in a MP spacetime is bound from above according to

$$\eta < \eta^b = -E_{(1)}^{\min}. \tag{2.56}$$

We remark that the upper bound above is a function of $\mu_{(1)}$, the break-up point coordinates ρ_* and z_*, and the MP parameters (M_1, M_2, and a). With the help of Eq. (2.48), we now investigate in detail how these quantities affect the efficiency bound.

The dependence of η^b on the charge-to-mass ratio $\mu_{(1)}$ is simple: η^b increases linearly with $\mu_{(1)}$. The dependence of η^b on the break-up point can be understood with the help of the energy levels shown in Fig. 2.5: the efficiency bound increases as the break-up point approaches either one of the black holes. A more detailed analysis is shown in Fig. 2.9, where we plot η^b as a function of z_* for selected values of ρ_* when $M_R = 1/2$, $M_T = 3$, and $\overline{\mu}_{(1)} = -5/4$ (corresponding to the energy levels shown in the middle panel of Fig. 2.5). Note that when the break-up point is outside the ergosphere, the efficiency bound becomes negative, meaning that the escaping fragment will carry away less energy than the incident particle had. The Penrose process is most efficient

if the break-up occurs exactly at either one of the event horizons, as indicated by the red dots in Fig. 2.9. When this happens, the upper bound is $-\mu_{(1)}$, which is in agreement with results obtained for the RN metric [40, 41].
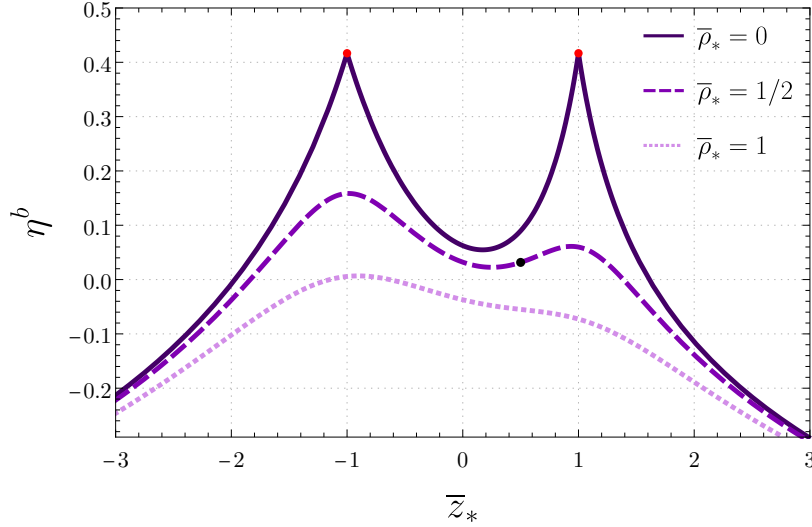
Figure 2.9: Efficiency bound η^b as a function of z_* for $\overline{\rho}_* = 0$ (solid curve), $\overline{\rho}_* = 1/2$ (dashed curve), and $\overline{\rho}_* = 1$ (dotted curve) when $M_R = 1/2$, $M_T = 3$, and $\overline{\mu}_{(1)} = -5/4$. The associated ergosphere corresponds to the point **E** in Figs. 2.3 and 2.4, while the associated energy levels are shown in the middle panel of Fig. 2.5. The red dots indicate the efficiency when the particle breaks-up at the black holes. The black dot shows the maximum efficiency $\eta^b = 0.03161$ for the processes represented in Fig. 2.13 and Tables 2.3 and 2.4.

To study the dependence of the efficiency bound on the masses of the black holes, we plot η^b as a function of the mass ratio M_R when $M_T/a = 3$ (top panel of Fig. 2.10) and as a function of M_T/a when $M_R = 1/2$ (top panel of Fig. 2.11). In both cases we have set the charge-to-mass ratio as $\mu_{(1)} = -5/12$. Each curve in these plots is associated with a different break-up point. The break-up points are shown in the bottom panels of Figs. 2.10 and 2.11. In the bottom panel of Fig. 2.10, we also exhibit the generalized ergosphere associated with a few selected values of M_R (which are chosen to reproduce the ergospheres labeled **D**, **E** and **F** in Figs. 2.3 and 2.4). Analogously, the ergospheres depicted in the bottom panel of Fig. 2.11 (and the associated values of M_T/a) correspond to the ergospheres labeled **B**, **E** and **H** in Figs. 2.3 and 2.4.

As shown in the top panel of Fig. 2.10, when the mass ratio M_R increases (while the other parameters are kept fixed), η^b will also increase if the break-up point is closer to the lighter black hole and will decrease if the break-up point is closer to the heavier black hole. This behavior is related to the fact that the growth of M_R produces an expansion of the ergosphere around the lighter companion and a reduction of the ergosphere around the heavier companion, as seen in the bottom panel of Fig. 2.10. Note that the efficiency bound is independent of the mass ratio if the break-up point is equidistant to the black holes. On the other hand, as shown in Fig. 2.11, when M_T/a increases (while the other parameters are kept fixed), the ergosphere expands and η^b increases. We note that in the limit $M_T/a \to \infty$, no matter where the break-up occurs, the efficiency bound approaches its maximum, i.e. $\eta^b \to -\mu_{(1)}$. This is explained by the fact that the distance between the break-up point and the black holes becomes negligible in comparison to the size of the ergosphere when $M_T/a \to \infty$.

Finally, we investigate the behavior of η^b when $\mu_{(1)}$ and M_T/a vary simultaneously, but their product, i.e. $\overline{\mu}_{(1)} = \mu_{(1)}M_T/a$, is kept fixed, meaning that the shape of the ergosphere is fixed (only the energy levels inside it change). In Fig. 2.12 we plot η^b as a function of $\mu_{(1)}$ and M_T/a for three different break-up points when $M_R = 1/2$ and $\overline{\mu}_{(1)} = -5/4$, so that the resulting ergosphere corresponds to the one labeled **E** in Figs. 2.3 and 2.4. The break-up points are chosen to be $(\overline{\rho}_*, \overline{z}_*) = (d, 1 - d)$, with $d = 1/2$, $d = 1/3$, and $d = 1/4$. We observe that, as $|\overline{\mu}|$ increases and M_T/a decreases, the efficiency bound increases, approaching an asymptotic value in the limit $\mu_{(1)} \to -\infty$ and $M_T/a \to 0$.

2.3.6 Examples

We now give concrete examples of energy extraction in a MP binary black hole spacetime whose efficiency approaches the theoretical maximum given by Eq. (2.56). The general procedure that we follow is outlined below. First, we choose the MP parameters M_1, M_2 and a. Second, we choose the charge-to-mass ratio $\mu_{(1)}$ and a break-up point (ρ_*, z_*, ϕ_*) that is inside the
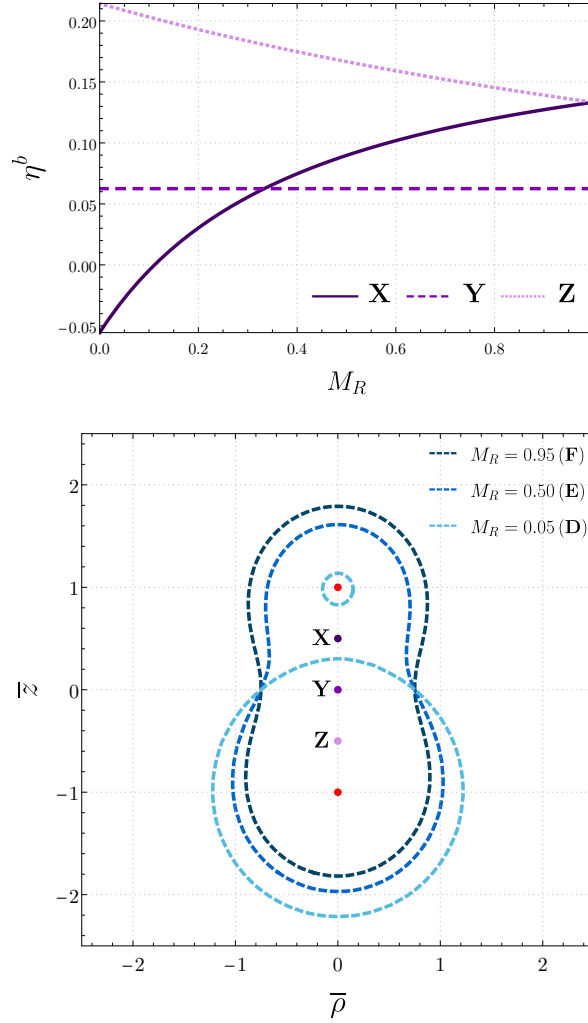
Figure 2.10: Top panel: efficiency bound η^b as a function of M_R when $M_T/a = 3$ and $\mu_{(1)} = -5/12$. Bottom panel: generalized ergosphere for selected values of M_R (corresponding to the points **D**, **E** and **F** in Fig. 2.3) when $M_T/a = 3$ and $\mu_{(1)} = -5/12$. The red dots indicate the location of the black holes. The purple dots are the locations of the break-up points $(\overline{\rho}_*, \overline{z}_*) = (1/2, 1/2)$, $(\overline{\rho}_*, \overline{z}_*) = (1/2, 0)$, and $(\overline{\rho}_*, \overline{z}_*) = (1/2, -1/2)$ and are labeled **X**, **Y** and **Z**, respectively. Each curve in the top panel corresponds to one of the break-up points shown in the bottom panel.

generalized ergosphere of the spacetime. Without loss of generality, we set $m_{(0)} = 1$.

Following the discussion leading to the inequality (2.56), we set $L_{(0)} =$
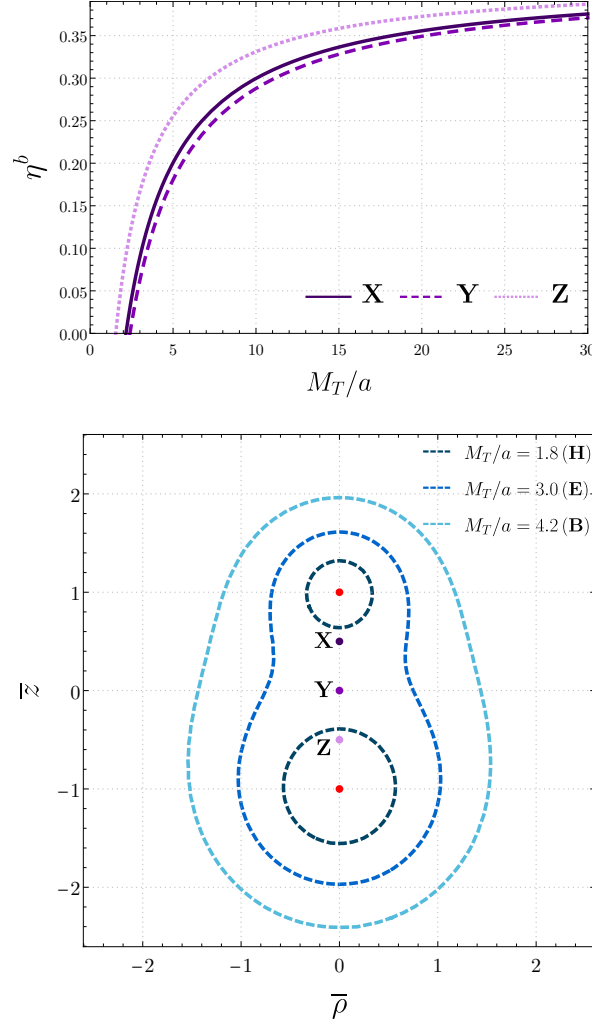
Figure 2.11: Top panel: efficiency bound η^b as a function of M_T/a when $M_R = 1/2$ and $\mu_{(1)} = -5/12$. Bottom panel: generalized ergosphere for selected values of M_T/a (corresponding to the points **B**, **E** and **H** in Fig. 2.3) when $M_R = 1/2$ and $\mu_{(1)} = -5/12$. The red dots indicate the location of the black holes. The purple dots are the locations of the break-up points $(\overline{\rho}_*, \overline{z}_*) = (1/2, 1/2)$, $(\overline{\rho}_*, \overline{z}_*) = (1/2, 0)$, and $(\overline{\rho}_*, \overline{z}_*) = (1/2, -1/2)$ and are labeled **X**, **Y** and **Z**, respectively. Each curve in the top panel corresponds to one of the break-up points shown in the bottom panel.

$L_{(1)} = L_{(2)} = 0$, meaning that all trajectories are restricted to the plane $\phi = \phi_*$. The energy $E_{(1)}$ is determined by Eq. (2.48), while $E_{(0)} = 1$. According to
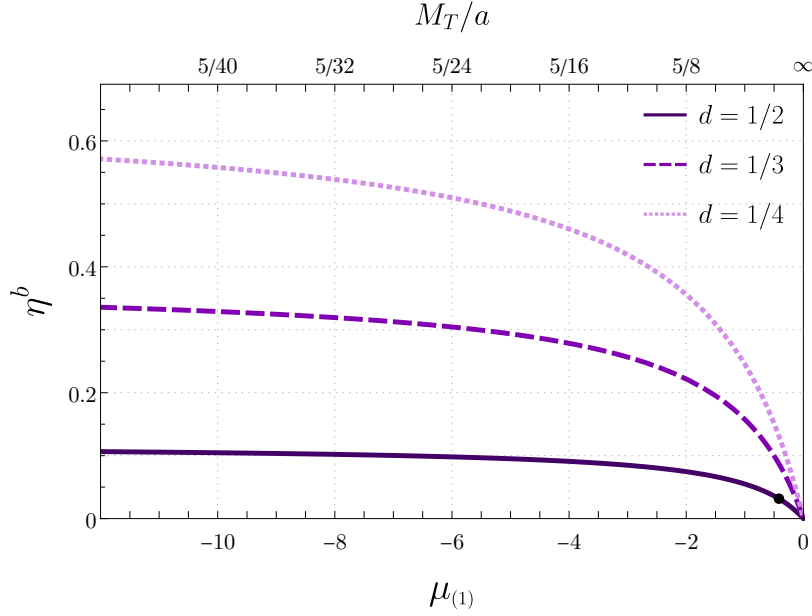
Figure 2.12: Efficiency bound η^b as a function of $\mu_{(1)}$ (bottom axis) and M_T/a (top axis) for $M_R = 1/2$ and $\overline{\mu}_{(1)} = -5/4$. The fact that $\overline{\mu}_{(1)}$ is fixed implies that $\mu_{(1)}$ and M_T/a are inversely proportional to each other. The curves, from bottom to top, correspond to the break-up points $(\overline{\rho}_*, \overline{z}_*) = (d, 1-d)$, with $d = 1/2$, $d = 1/3$, and $d = 1/4$ respectively. The black dot shows the maximum efficiency $\eta^b = 0.03161$ for the processes represented in Fig. 2.13 and Tables 2.3 and 2.4, i.e. when $d = 1/2$, $\mu_{(1)} = -5/12$ and $M_T/a = 3$.

Eqs. (2.53) and (2.55), we choose

$$\mu_{(0)} = 1 - \varepsilon, \tag{2.57}$$

$$m_{(1)} = 1 - \nu, \tag{2.58}$$

where ε and ν are small positive parameters satisfying

$$\nu > \varepsilon(U_* - 1)\left(\sqrt{1 + \frac{2}{\varepsilon(U_* - 1)}} - 1\right). \tag{2.59}$$

Since $m_{(1)}$ has been fixed, the mass $m_{(2)}$ can be determined by Eq. (2.50). The quantities $\mu_{(2)}$ and $E_{(2)}$ are determined from Eqs. (2.40) and (2.42), respectively.

At the break-up point, according to Eq. (2.47), we have $\dot{\rho}_{(1)} = \dot{z}_{(1)} = 0$ for

the negative energy fragment. For the incident particle, on the other hand, the choices for $\mu_{(0)}$ and $E_{(0)}$ imply that

$$\dot{\rho}_{(0)}^2 + \dot{z}_{(0)}^2 = \varepsilon \frac{U_* - 1}{U_*^2} \left[2 + \varepsilon (U_* - 1) \right]. \tag{2.60}$$

By choosing the angle $\theta_{(0)} = \text{Arg} \left(\dot{\rho}_{(0)} + i \dot{z}_{(0)} \right)$ between the velocities $\dot{\rho}_{(0)}$ and $\dot{z}_{(0)}$, equation Eq. (2.60) can be used to determine $\dot{\rho}_{(0)}$ and $\dot{z}_{(0)}$ individually at the break-up point. The conservation of linear momentum then fixes the values of $\dot{\rho}_{(2)}$ and $\dot{z}_{(2)}$ through Eq. (2.43). At this point, the trajectories $T_{(0)}$, $T_{(1)}$, and $T_{(2)}$ have all been determined and the efficiency of the associated Penrose process is $\eta = (1 - \nu)\eta^b$. In order to maximize the efficiency of the Penrose process, one must, therefore, set η to be as small as possible. Note, however, that one cannot choose $\varepsilon = 0$, because this would imply $\dot{\rho}_{(0)} = \dot{z}_{(0)} = 0$ and $\ddot{\rho}_{(0)} = \ddot{z}_{(0)} = 0$ at the break-up point, contradicting the fact the trajectory $T_{(0)}$ starts infinitely far away. Similarly, ν cannot be chosen to saturate inequality (2.59), otherwise $m_{(2)}$ would be exactly zero, contradicting the fact that all trajectories are time-like. If desired, this can be remedied by assuming, from the start, that the escaping fragment is massless (however, this would modify Eq. (2.31) and the present analysis). Nevertheless, it is possible, in principle, to have infinitesimally small values for ε and ν. Finally, we point out that not every angle θ_0 produces trajectories that are consistent with the assumptions of a Penrose process. More precisely, only certain ranges of θ_0 give rise to trajectories $T_{(0)}$ and $T_{(2)}$ that, respectively, start and end infinitely far away from the black holes.

i	$m_{(i)}$	$\mu_{(i)}$	$E_{(i)}$	$L_{(i)}$	$\dot{\rho}_{(i)}$	$\dot{z}_{(i)}$
0	1.00000	0.99990	1.00000	0	0.00609	0.00158
1	0.90000	-0.41667	-0.03161	0	0.00000	0.00000
2	0.09756	14.09301	10.54183	0	0.06243	0.01621

Table 2.3: Parameters that generate the trajectories $T_{(0)}$, $T_{(1)}$, and $T_{(2)}$ of the Penrose process shown in the left panel of Fig. 2.13. The derivatives $\dot{\rho}_{(i)}$ and $\dot{z}_{(i)}$ are evaluated at the break-up point.

We conclude by showing in Fig. 2.13 two explicit examples of the procedure
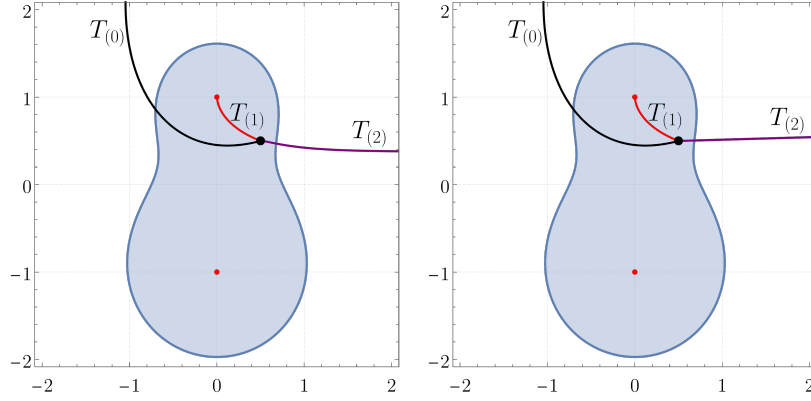
Figure 2.13: Examples of Penrose processes that approach the maximum theoretical efficiency in a MP spacetime. The efficiencies of the processes in the left and right panel are, respectively, 90% and 99% of the theoretical maximum. In both cases the incoming trajectory $T_{(0)}$ (black curve) splits at the black point into the negative energy orbit $T_{(1)}$ (red curve) and the trajectory of the escaping fragment $T_{(2)}$ (purple curve). The parameters that generate these trajectories are shown in Tables 2.3 and 2.4. The blue region is the generalized ergosphere (for particle 1) and the red dots indicate the location of the black holes.

outlined above for the MP spacetime with $M_1 = 2$, $M_2 = 1$, and $a = 1$. The charge-to-mass ratio of the negative energy fragment is chosen as $\mu_{(1)} = -5/12$, so that the associated generalized ergosphere is the one identified by the letter **E** in Figs. 2.3 and 2.4. The break-up point is chosen as $(\rho_*, z_*) = (1/2, 1/2)$, fixing the trajectory $T_{(1)}$ and its energy (per unit mass) $E_{(1)} = -0.03161$ (remember that the initial conditions are chosen so that $E_{(1)}$ is the minimum possible). According to Eq. (2.56), the efficiency bound is $\eta^b = 0.03161$ (which corresponds to the black dots in Figs. 2.9 and 2.12). The trajectories $T_{(0)}$ and $T_{(2)}$ are specified by the choices of ε, ν, and $\theta_{(0)}$. In the left panel of Fig. 2.13 we exhibit the Penrose process for $\varepsilon = 10^{-4}$, $\nu = 10^{-1}$, and $\theta_{(0)} = 0.25403$, whose efficiency is 90% of the theoretical maximum. In the right panel of Fig. 2.13 we exhibit the Penrose process for $\varepsilon = 10^{-5}$, $\nu = 10^{-2}$, and $\theta_{(0)} = 0.25403$, whose efficiency is 99% of the theoretical maximum. The parameters that generate these examples and satisfy Eqs. (2.40)-(2.45) are given in Tables 2.3 and 2.4.

i	$m_{(i)}$	$\mu_{(i)}$	$E_{(i)}$	$L_{(i)}$	$\dot{\rho}_{(i)}$	$\dot{z}_{(i)}$
0	1	0.99999	1.00000	0	0.00193	0.00050
1	0.99000	-0.41667	-0.03161	0	0.00000	0.00000
2	0.00685	206.13521	150.50460	0	0.28104	0.07297

Table 2.4: Parameters that generate the trajectories $T_{(0)}$, $T_{(1)}$, and $T_{(2)}$ of the Penrose process shown in the right panel of Fig. 2.13. The derivatives $\dot{\rho}_{(i)}$ and $\dot{z}_{(i)}$ are evaluated at the break-up point.

2.4 CMMR Spacetime

We now consider the extension of the results presented in Sec. 2.3 to a binary system of rotating black holes described by the CMMR metric. In Weyl's cylindrical coordinates, the CMMR line element reads

$$
ds^2 = -f(\rho, z) \left[dt - \omega(\rho, z) d\phi \right]^2
$$
$$
+ f(\rho, z)^{-1} \left[e^{2\gamma(\rho, z)} \left(d\rho^2 + dz^2 \right) + \rho^2 d\phi^2 \right], \quad (2.61)
$$

where the real valued functions $f(\rho, z)$, $\omega(\rho, z)$ and $\exp[2\gamma(\rho, z)]$ are defined as in Sec. IV of Ref. [25]. As in the case of the MP metric, only the exterior of the black holes is described by these coordinates. In particular, the outer event horizons of the constituent black holes are straight lines in these coordinates (see Fig. 2.14).

The CMMR solution is fully characterized by five independent parameters, namely the masses $M_{1,2}$, the angular momenta per unit mass $a_{1,2}$ and the coordinate distance R between the black hole centers. From these, we define three additional parameters, namely $M_T = M_1 + M_2$, which represents the total mass of the system, $J_T = M_1 a_1 + M_2 a_2$, which represents the total angular momentum of the system, and a_*, which is a root of the cubic equation

$$
\left(R^2 - M_T^2 + a_*^2 \right) \left(a_1 + a_2 - a_* \right) + 2 \left(R + M_T \right) \left(J_T - M_T a_* \right) = 0. \quad (2.62)
$$

We note that, depending on the parameters, the CMMR metric can represent a black hole-black hole binary, a naked singularity-naked singularity binary, or a black hole-naked singularity binary [23, 24, 25]. In our analysis, the chosen

45

parameters always correspond to a binary black hole solution. In practice, this means that the chosen parameters must:

1. Produce real valued and positive horizon lengths. The horizon half-lengths are given by the expressions σ_1 and σ_2 in Sec. IV of Ref. [25].

2. Produce horizons that do not touch or overlap.

3. Produce a single real root for a_* in Eq. (2.62).

2.4.1 Geodesics

Once again, we will make use of the Lagrangian formalism to determine the geodesic equations and the conserved quantities corresponding to the symmetries of the system. The Lagrangian associated with the geodesic motion of a massive and neutral test particle in the CMMR metric is [42]

$$2\mathcal{L} = -f(\dot{t} - \omega\dot{\phi})^2 + f^{-1}\left[e^{2\gamma}\left(\dot{\rho}^2 + \dot{z}^2\right) + \rho^2\dot{\phi}^2\right], \tag{2.63}$$

where, once again, dots represent derivatives with respect to the proper time λ.

Due to the stationarity and the axisymmetry of the system, we can identify two constants of the motion analogous to the quantities defined in Eqs. (2.28) and (2.29). The energy per unit mass, as measured by a static observer at infinity, is given by

$$E = f\dot{t} - \omega f\dot{\phi}, \tag{2.64}$$

and the angular momentum (with respect to the z axis) per unit mass, as measured by a static observer at infinity, is given by

$$L = \omega f\dot{t} + \left(\frac{\rho^2}{f} - \omega^2 f\right)\dot{\phi}. \tag{2.65}$$

Using Eqs. (2.64) and (2.65) to eliminate $\dot{t}$ and $\dot{\phi}$ from the normalization of the four velocity, i.e. $\dot{x}^\mu\dot{x}_\mu = -1$, we obtain an expression for the energy E in

terms of $\dot{\rho}$, $\dot{z}$ and the angular momentum L:

$$E = \frac{-f^2\omega L}{\rho^2 - \omega^2 f^2} + \left[\frac{\rho^2 e^{2\gamma}(\dot{\rho}^2 + \dot{z}^2)}{\rho^2 - \omega^2 f^2} \right.$$
$$\left. + \left(\frac{\rho f L}{\rho^2 - \omega^2 f^2} \right)^2 + \frac{\rho^2 f}{\rho^2 - \omega^2 f^2} \right]^{1/2}, \tag{2.66}$$

where the positive sign is once again chosen for the square root in order to guarantee that a static particle at infinity has positive energy. We rewrite the equation above as Eq. (2.32), where the effective energy and the effective potential are now given by

$$V_{\text{eff}} = \frac{\rho^2 - \omega^2 f^2}{\rho^2 e^{2\gamma}} \left[\left(\frac{\rho f L}{\rho^2 - \omega^2 f^2} \right)^2 + \frac{\rho^2 f}{\rho^2 - \omega^2 f^2} \right] \tag{2.67}$$

and

$$E_{\text{eff}} = \frac{\rho^2 - \omega^2 f^2}{\rho^2 e^{2\gamma}} \left(E + \frac{f^2\omega L}{\rho^2 - \omega^2 f^2} \right)^2. \tag{2.68}$$

Note that the constraints given in Eq. (2.35) also apply to Eqs. (2.67) and (2.68).

The geodesic equations, analogous to Eqs. (2.36) and (2.37), can be derived from the Euler-Lagrange equations for the Lagrangian (2.63). Their explicit forms, in terms of E, L and the metric functions f, ω and $e^{2\gamma}$, are given in Eqs. (16) and (17) of Ref. [42]. Once $\rho(\lambda)$ and $z(\lambda)$ are known, $t(\lambda)$ and $\phi(\lambda)$ are determined by direct integration of Eqs. (2.64) and (2.65).

2.4.2 Ergosphere

Since the CMMR metric is stationary, and we are considering neutral particles in geodesic motion, we use the standard definition of an ergosphere to study the possibility of negative energy orbits and energy extraction. In other words, the ergosphere is the region where the time translation Killing vector field becomes space-like, i.e. $(\partial_t)^\mu (\partial_t)_\mu > 0$. Taking into account the line element (2.61), it is straightforward to show that the ergosphere of the CMMR spacetime is the

47

locus of points that satisfy

$$f(\rho, z) < 0. \tag{2.69}$$

We sketch this ergosphere in Fig. 2.14, where each panel is labeled by a letter (**A-I**) and corresponds to a different set of parameters (which are specified in Table 2.5). In each panel, the blue shaded region represents the $\phi = 0$ section of the ergosphere, while the red lines represent the event horizons of the black holes. The top row of the figure (panels **A-C**) exhibits the effect of changing the mass ratio of the system while keeping the total mass, both spins and the separation parameter fixed. It shows that, analogously to the MP case, initially disjoint ergospheres may merge into a single connected ergosphere when the mass ratio increases. The middle row of Fig. 2.14 (panels **D-E**), on the other hand, shows the effect of changing the spin parameter of the top black hole while keeping all other parameters fixed. We observe that when initially aligned spins become anti-aligned, the ergosphere becomes thinner and elongated along the symmetry axis. Finally, the bottom row (panels **G-H**) illustrates the effect of increasing the separation parameter when all other parameters are kept fixed. Similarly to what happens in the MP case, if the distance between the black holes is sufficiently large, there will be two disconnected ergospheres, one for each black hole.

Panel	M_1/M_2	a_1/M_T	a_2/M_T	R/M_T
A	0.16	0.65	0.65	1.00
B	0.58	0.65	0.65	1.00
C	1.00	0.65	0.65	1.00
D	1.00	0.50	0.65	1.00
E	1.00	0.30	0.65	1.00
F	1.00	−0.10	0.65	1.00
G	1.00	0.65	0.65	1.11
H	1.00	0.65	0.65	1.30
I	1.00	0.65	0.65	2.00

Table 2.5: Parameters that define the CMMR metrics associated with the ergospheres **A-I** shown in Fig. 2.14.
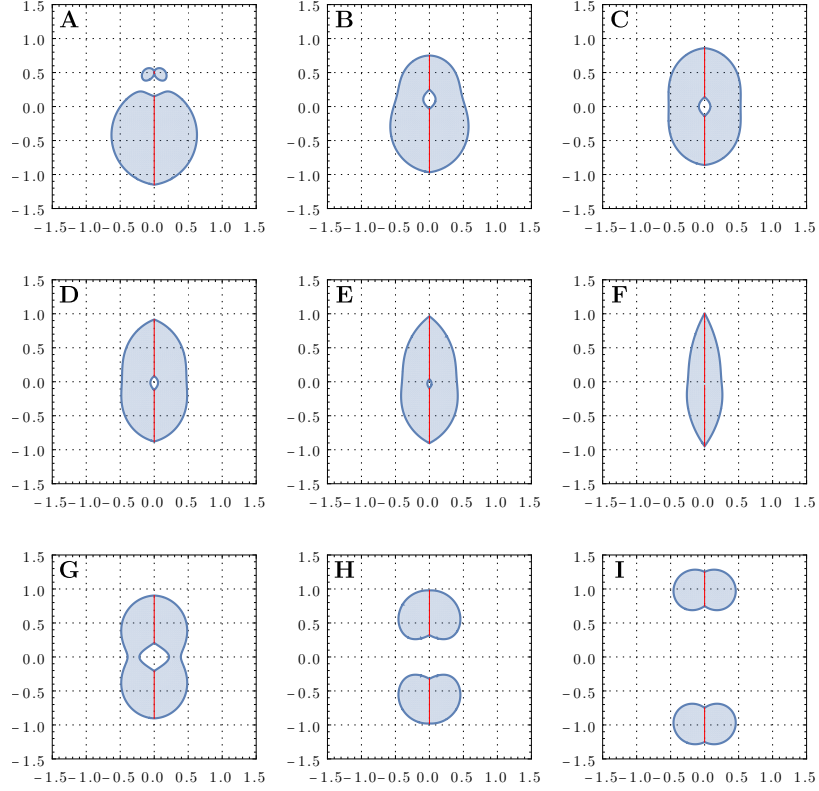
Figure 2.14: The $\phi = 0$ section of the ergosphere of the CMMR metric for different set of parameters labeled **A-I** (see Table 2.5). In each plot the horizontal and vertical axes are ρ/M_T and z/M_T, respectively. The red lines indicate the location of the black hole's horizons.

2.4.3 Bound negative energy orbits and the Penrose Process

To demonstrate the existence of bound negative energy orbits and the possibility of using them to extract energy from non-coalescing Kerr binaries, we shall restrict our attention to systems of equal mass and spin. This symmetry allows for the existence of stable orbits (in the sense already discussed for the MP metric) in the $z = 0$ plane. To find a negative energy trajectory that is confined outside the black holes, we choose the energy E and the angular momentum L such that there are two orbital turning points of Eq. (2.32) that lie inside the ergosphere of the system. Similarly to what was done in the MP case, once the initial radius $\rho(0)$, the energy, and the angular momentum are fixed, we solve Eq. (2.66) to determine $\dot{\rho}(0)$ and integrate the geodesic equations. Using

the parameters that produce the ergosphere **C** of Fig. 2.14 and Table 2.5, we show an example of such a negative energy orbit in Fig. 2.15 (right panel). The corresponding effective potential and effective energy are also shown in Fig. 2.15 (left panel).
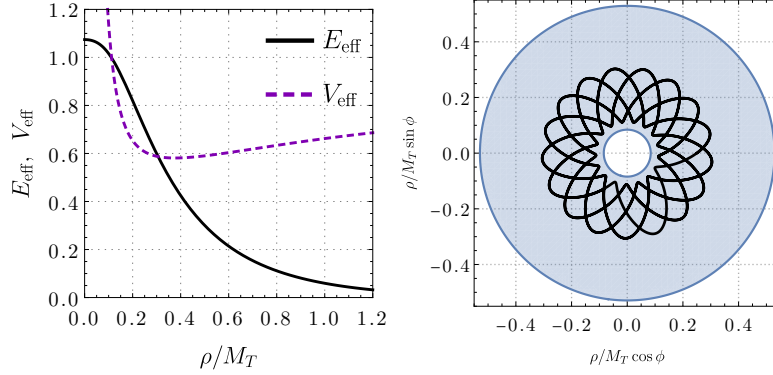
Figure 2.15: Left panel: effective energy (black curve) and effective potential (purple dashed curve) for $L = -2.5$ and $E = -0.054$, when the CMMR metric is characterized by $a_1 = a_2 = 0.65$, $M_1 = M_2 = 0.5$, and $R = 1$ (corresponding to the label **C** in Table 2.5). The turning points are located at $\rho_-/M_T = 0.112531$ and at $\rho_+/M_T = 0.306081$. Right panel: the associated trajectory in the $z = 0$ plane when $\rho(0)/M_T = 0.25$ and $\phi(0) = 0$. The blue region is the $z = 0$ section of the ergosphere of the spacetime.

Adopting the same notation introduced Sec. 2.3 for the trajectories in a Penrose process around the MP black hole, and taking advantage of the negative energy orbit depicted in Fig. 2.15, we now consider the possibility of energy extraction in the CMMR spacetime. By employing the conservation of 4-momentum (as in Sec. III), we construct an explicit example of a Penrose process. The obtained trajectories are shown in Fig. 2.16 and the corresponding parameters are given in Table 2.6. The efficiency of the process, calculated through Eq. (2.46), is $\eta \approx 0.08\%$.

2.5   Non-Stationary Spacetimes

In the previous sections, all of our considerations depended upon the existence of a conserved negative and "global" (as seen by a static observer at infinity)
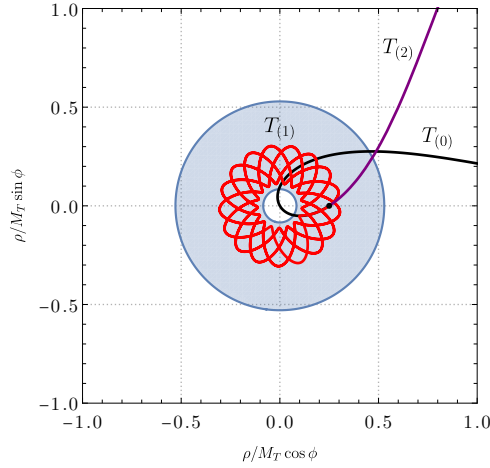
Figure 2.16: Penrose's process in the $z = 0$ plane of a CMMR spacetime with $M_1 = M_2 = 0.5$, $a_1 = a_2 = 0.65$, and $R = 1$. The incoming trajectory $T_{(0)}$ (black curve) splits at the black point ($\rho/M_T = 0.25$, $\phi = 0$) into the negative energy orbit $T_{(1)}$ (red curve) and the trajectory of the escaping fragment $T_{(2)}$ (purple curve). The parameters that generate these trajectories are shown in Table 2.6. The blue region is the $z = 0$ section of the ergosphere (for particle 1).

energy. This is only possible if the spacetime under consideration is stationary. In this section we will demonstrate how one can still observe the Penrose Process even in cases where this assumption is relaxed and there is no global and conserved energy available to be explored, thus, looking only at locally defined quantities. This technique allows one to study the Penrose mechanism even when the spacetime metric is defined numerically, such as is the case in numerical simulations of binary black hole collisions.

2.5.1   3+1 split of the geodesic equation

To understand our proposed technique, it is first fundamental to understand how General Relativity can be reformulated by explicitly separating its spatial and temporal components. This decomposition know as a "3+1 split" is very commonly used in Numerical Relativity and was motivated by the first attempts of posing GR as a Cauchy problem. Numerical Relativity codes very often provide ways to access the spacetime metrics being evolved in terms of it's 3+1 components. In this section, we will assume familiarity of the reader with

i	$m_{(i)}/m_0$	$E_{(i)}$	$L_{(i)}$	$\dot{\rho}_{(i)}$	$\dot{z}_{(i)}$
0	1.0000000	2.00000	0.000000	4.343904	0
1	0.0289697	-0.05400	-2.500000	0.313887	0
2	0.3148980	6.35623	0.229993	13.765800	0

Table 2.6: Parameters that generate the trajectories $T_{(0)}$, $T_{(1)}$, and $T_{(2)}$ of the Penrose process shown in Fig. 2.16. The derivatives $\dot{\rho}_{(i)}$ and $\dot{z}_{(i)}$ are evaluated at the break-up point.

this concept which can be readily reviewed in Refs. [43, 44, 45]. Given that the Penrose process requires us to investigate the trajectories of particles in a background spacetime, we must now solve the geodesic equation taking into account that the spacetime metric (and it's derivatives) will be provided via 3+1 split components. The need to solve the geodesic equation in this context overlaps with works that are interested in simulating an image of a black hole, that is, determining what a camera would capture if it was pointed towards one. In this type of simulation a technique called *backwards ray tracing* is employed, which consists in choosing a position and orientation of a model camera and integrating the trajectory of the photons that hit the camera's "film" backwards in time. The color of each pixel in the resulting image is then computed by analyzing whether the particle was swollen or the color of the "obstacle" that it hit.

Although our purposes differ, the mathematical tools used in backwards ray tracing are fundamental in the technique we will soon develop. The complete and detailed derivation of the 3+1 split of the geodesic equation used in this section can be found in Ref. [46]. We shall recover from this reference only the nomenclatures and concepts necessary for the further development of our proposal. To begin with, we consider a globally hyperbolic background spacetime described by a metric tensor $g_{\mu\nu}$. Being globally hyperbolic, it admits a one parameter space-like foliation of constant coordinate time t hypersurfaces that we shall denote by Σ_t. We will also assume that the space-time has coordinates[2] that are compatible with the foliation, that is, $x^0 = t$ and x^i span

---

[2]We use the convention that Greek indices run over all 4 coordinates while Latin indices run

Σ_t. Let us denote the unit time-like (future directed) normal vector of Σ_t by n^μ. This vector coincides with the 4-velocity of an observer whose worldlines are orthogonal to Σ_t, which we call the *Eulerian Observer*, or O_E. We denote by $\gamma_{\mu\nu}$ the spatial metric induced in Σ_t, D_i its associated covariant derivative, K_{ij} its extrinsic curvature tensor, N the lapse function and β^μ the shift vector. The 3+1 split metric then becomes

$$ds^2 = -N^2 dt^2 + \gamma_{ij}(dx^i + \beta^i dt)(dx^j + \beta^j dt). \tag{2.70}$$

Let us now consider a particle $\mathcal{P}$ of 4-momentum p^μ. Let us assume that the particle moves in either a time-like or null geodesic (and thus without the influence of any force but gravity), which implies that

$$p_\mu p^\mu = m^2 \delta, \tag{2.71}$$

where $\delta = -1$ for massive particles (and in this case m represents the particle's mass) or $\delta = 0$ for photons. The 4-momentum can be decomposed as

$$p^\mu = E(n^\mu + V^\mu) \tag{2.72}$$

where E represents the particle's energy as measured by O_E (by definition, $E = -n_\mu p^\mu$) and V^μ represents the 3-velocity of the particle, also as measured by O_E. The 3-momentum P^μ of $\mathcal{P}$ as observed by O_E is thus

$$P^\mu \equiv \gamma^\mu{}_\nu p^\nu = E V^\mu. \tag{2.73}$$

The normalization of p^μ and n_μ, together with the orthogonality relation $n_\mu V^\mu = 0$ and Eq. (2.72) imposes

$$V_\mu V^\mu = V_i V^i = 1 + \delta \left(\frac{m}{E}\right)^2. \tag{2.74}$$

Finally, parametrizing the particle's position vector X^i by the coordinate time (that is $x^i = X^i(t)$) the geodesic equation of $\mathcal{P}$ is decomposed in a set of 7

---

over only spatial coordinates.

equations, namely

$$\frac{\mathrm{d}X^i}{\mathrm{d}t} = NV^i - \beta^i \tag{2.75}$$

$$\frac{\mathrm{d}V^i}{\mathrm{d}t} = NV^j \left[V^i \left(\partial_j \ln N - K_{jk} V^k \right) + 2K^i{}_j - {}^3\Gamma^i_{jk} V^k \right] - \gamma^{ij} \partial_j N - V^j \partial_j \beta^i \tag{2.76}$$

$$\frac{\mathrm{d}E}{\mathrm{d}t} = E(NK_{jk} V^j V^k - V^j \partial_j N) \tag{2.77}$$

where ${}^3\Gamma^i_{jk}$ are the Christoffel symbols associated with γ_{ij}.

2.5.2 Penrose process

Eq. (2.77) gives us the time evolution of the energy as measured by the Eulerian Observer when the particle travels along its path. From here on, we will refer to this quantity as the *local energy*, since it is measured locally by the observer that is orthogonal to the foliation and denote it by E. Up until now, we've been dealing with what we shall now call the *global energy*, that is, the energy as measured by a static observer at infinity, that we will now denote by ε. Our study will require, further on, that we find a relation between these two quantities, so we shall do so now. The global energy, ε, is given when the spacetime under consideration possesses a global time-like Killing vector field $\xi^\mu = (\partial_t)^\mu$ and is defined as

$$\varepsilon = p_\mu \xi^\mu. \tag{2.78}$$

Expanding the contraction in Eq. (2.78) with the general metric given in Eq. (2.70) and with the 4-momentum given in Eq. (2.72), we get

$$\varepsilon = \left(N - \gamma_{ij} \beta^i V^j \right) E. \tag{2.79}$$

Previously, we were able to determine if energy was extracted as a result of a particle split-up process by comparing the global energies of the particles involved, one of which must have had a negative energy value. Since global energy was conserved along the particle's trajectories, it did not matter where and when this comparison took place. If we, however, relax the assumption that the spacetime under analysis possesses a global time-like killing vector

field, the quantity given by Eq. (2.78) is no longer physically meaningful as an energy measure, thus restricting all physical arguments to be made in terms of local energy measurements. Furthermore, local energy, as can be explicitly seen in Eq. (2.77), is not in general conserved along the particle's trajectory and must always be positive in order to be physically meaningful. Given these restrictions, how can one compare the local energies of the particles involved in a breakup (or collisional) process in a physically meaningful way in order to determine if energy was extracted from the system or not? To answer this question, one must note that there is an important consequence of Eq. (2.79) to be observed if the spacetime metric is asymptotically flat, that is, if infinitely far away from the black hole (or holes) the spacetime becomes the Minkowski solution. In this case, when spatial coordinates tend to infinity, $\gamma_{ij} \rightarrow \eta_{ij}$, $\beta^i \rightarrow 0$ and $N \rightarrow 1$ which implies, via Eq. (2.79), that $\varepsilon = E$. In other words, if the spacetime under consideration is asymptotically flat, global and local energy coincide at infinity, thus implying that the global energy is still physically meaningful infinitely far away from the gravitational center. Not only that, Eq. (2.77) tells us that local and global energies are conserved at infinity, since $K_{ij} \rightarrow 0$ and N becomes constant as we approach the Minkowski solution.

In practical terms (and especially when analyzing spacetime metrics obtained from numerical simulation codes) it's not possible to integrate a trajectory to spatial infinity since the coordinates commonly employed are not compactifyied and such compactification is often difficult or impossible to perform in practice. Instead of attempting to do so, our technique follows again a practice common in backward ray tracing works, more specifically, we follow the prescription given by Ref. [19]. Given a set of initial conditions $X^i(0), V^i(0), E(0)$, we evolve the system formed by Eqs. (2.75)-(2.77) numerically until the particle reaches a sphere of predetermined radius that we denominate the *background sphere*. The radius of this sphere is chosen so that the difference between global and local energy becomes smaller than a certain threshold δ_E, that is,

$$|E(t_f) - \varepsilon(t_f)| < \delta_E, \tag{2.80}$$

where t_f represents the final integration coordinate time. Additionally, we also

stop integrating if the particle is absorbed by the system at a given time of "swallowing" t_S. A particle is considered absorbed if the difference of its local energy at t_S and at $t = 0$ gets larger than a certain swallowing threshold δ_S, that is,

$$|E(t_S) - E(0)|/E(0) = \delta_S. \tag{2.81}$$

The scheme described above was implemented in a public C++ code available in Ref. [47]. Compilation and usage instructions are provided within the repository. The code was originally created with the intent of producing Gravitational Lensing images (hence the name) but was later adapted to investigate the Penrose process. The code consists of a *kernel* using the ARKODE [48] infrastructure for integrating the geodesic equation and verifying the stopping criteria of Eqs. (2.80) and (2.81) for an arbitrary spacetime metric. The kernel expects only to receive a set of functions that compute the ADM quantities of the spacetime metric (lapse, shift, extrinsic curvature and a few derivatives of these objects). Each spacetime metric is then a *plugin* (a dynamically loaded library) that provides such functions at runtime. This allows the integration problem be separated of the problem of determining the ADM quantities of a given spacetime metric. Users can focus on the latter, since the kernel solves the former for an arbitrary input metric. In addition to spacetime metrics being plugins, file readers and writers are also plugins in the same way. This allows the user to implement different input/output data formats for the trajectories according to their needs. Currently, only a simple ASCII file writer is available, but that is enough for our current purposes. The behavior of the program is driven at runtime by a command line interface, YAML configuration files and the available dynamic libraries implementing spacetime metrics and writers. A basic configuration file named grlensing_config.yaml is expected to be present, detailing various ARKODE internal settings, such as error tolerances, max. number of iterations, etc. It also details the metric and file writer plugins to be loaded and made available at runtime as well as settings of the dump-metric command. Additional configuration files are required in certain modes (for instance, describing a certain spacetime parameters and initial conditions of a particle). Through the command line, the user selects

the operation mode of the code. At the time of writing, the available modes of operation are (these can be viewed by invoking the program with `--help`)

- `list-plugins`: Lists all the plugins that are set to be loaded (and were found)

- `dump-metric`: Writes a spacetime metric in a cube of arbitrary size and arbitrary number of internal points. This option is used mostly for debugging the implementation of a spacetime metric plugin.

- `integrate-trajectory`: Integrates a single particle trajectory with the specified configurations.

- `penrose-breakup`: Integrates a particle breakup process by using two particle configurations and obtaining a third from conservation of 4-momentum.

The general workflow for finding explicit examples of the Penrose process is as follows:

1. Chose a break-up point. This will be the initial position of all three particle participating in the process. We know that in order to extract energy this break-up must occur inside the ergosphere. In general, when the spacetime under study does not possess a global time-like killing vector field, we consider the ergosphere to be the now observer dependent region where the metric component g_{tt} changes sign.

2. Chose initial velocities and energy for the ingoing particle in such a way that it is an escaping orbit when integrated forward and backward in time. Requiring that the orbit is escaping in both "temporal directions" makes it more likely that one of the particles produced after the break-up will escape to infinity.

3. Choose initial velocities and energy for the particle that is absorbed by the black whole and will be the equivalent of the negative energy orbit. These parameters are chosen so that the particle is counter-rotating with the black whole that will absorb it, so that its angular momentum can actually be decreased upon absorption.

4. The escape orbit parameters are computed automatically by the code via 4-momentum conservation at the break-up point.

Several utility scripts are also provided in the program repository under the `resources` folder. These scripts serve multiple purposes, from plotting trajectories, energies, the ADM quantities of dumped spacetime metrics or even generating a skeleton of a metric plugin that can be filled by users. It also includes an assortment of papers and notes required in the development of the code.

2.5.3   Parametrizing initial velocities

As was previously mentioned, we must choose 7 parameters in order to solve the 3+1 split geodesic equation. Once initial positions $X^i(0)$ and local energy $E(0)$ values are chosen one is still free to choose 3 initial velocity $V^i(0)$ values. We have chosen to consider only orbits in the $z = 0$ plane, which implies $V^3(0) = 0$. We do not believe that this choice represents a loss of generality since it is valid for all cases of interest, including astrophysical black hole binaries. By comparing Eq. (2.74) to a general bi-variate quadratic form

$$AX^2 + 2BXY + CY^2 + 2DX + 2FY + G = 0, \tag{2.82}$$

it is possible to identify

$$A = \gamma_{22},\, B = \gamma_{23},\, C = \gamma_{33},\, G = -\left[1 - \left(\frac{m}{E}\right)^2\right],\, D = F = 0, \tag{2.83}$$

and the variables X and Y with V^1 and V^2, respectively. This quadratic describes a non-degenerate real ellipse in the V^1-V^2 plane centered around $V_\circ^1$ and $V_\circ^2$ with semi-axis lengths $\alpha_\pm$ and counterclockwise angle ϕ of rotation from the V^1 axis to it's semi-major axis if after defining [49]

$$\Delta = \begin{vmatrix} A & B & D \\ B & C & F \\ D & F & G \end{vmatrix} = \left(1 - \left(\frac{m}{E}\right)^2\right)\left(\gamma_{23}^2 - \gamma_{22}\gamma_{33}\right), \tag{2.84}$$

$$J = \begin{vmatrix} A & B \\ B & C \end{vmatrix} = \gamma_{22} + \gamma_{33} - \gamma_{23}^2 \tag{2.85}$$

and

$$I = A + C = \gamma_{22} + \gamma_{33}, \tag{2.86}$$

one has $\Delta \neq 0, J > 0, \Delta/I < 0$ and $\gamma_{22} \neq \gamma_{33}$. Explicitly, we have [50, 51, 52]

$$V_\circ^1 = V_\circ^2 = 0, \tag{2.87}$$

$$\alpha_\pm = \sqrt{\frac{2\left(1 - (m/E)^2\right)}{\gamma_{22} \mp \sqrt{4\gamma_{23}^2 + (\gamma_{22} - \gamma_{33})^2} + \gamma_{33}}} \tag{2.88}$$

and

$$\phi = \begin{cases} 0 & \text{if } \gamma_{23} = 0 \text{ and } \gamma_{22} < \gamma_{33} \\ \frac{\pi}{2} & \text{if } \gamma_{23} = 0 \text{ and } \gamma_{22} > \gamma_{33} \\ \frac{1}{2}\cot^{-1}\left(\frac{\gamma_{22}-\gamma_{33}}{2\gamma_{23}}\right) & \text{if } \gamma_{23} \neq 0 \text{ and } \gamma_{22} < \gamma_{33} \\ \frac{\pi}{2} + \frac{1}{2}\cot^{-1}\left(\frac{\gamma_{22}-\gamma_{33}}{2\gamma_{23}}\right) & \text{if } \gamma_{23} \neq 0 \text{ and } \gamma_{22} > \gamma_{33} \end{cases}. \tag{2.89}$$

With these quantities, it is possible to describe the ellipse in terms of an arbitrary parameter $\Theta \in [0, 2\pi]$, that is,

$$V^1(\Theta) = V_\circ^1 + \alpha_+ \cos\Theta \cos\phi - \alpha_- \sin\Theta \sin\phi \tag{2.90}$$

$$V^2(\Theta) = V_\circ^2 + \alpha_- \sin\Theta \cos\phi + \alpha_+ \cos\Theta \sin\phi, \tag{2.91}$$

and thus the problem of finding initial velocities that satisfy Eq. (2.74) is reduced to that of evaluating the right-hand side of Eqs. (2.90) - (2.91) for some value of Θ, effectively reducing the "degrees of freedom" of the problem.

2.5.4 Kerr Metric

As an illustrative example and proof of concept, we will demonstrate the procedure described so far applied to the Kerr metric. In Kerr-Schild

coordinates (t, x, y, z), the metric components are given by [53]

$$g_{\mu\nu} = \eta_{\mu\nu} + 2Hl_\mu l_\nu, \tag{2.92}$$

where

$$H = \frac{Mr^3}{r^4 + a^2 z^2}, \tag{2.93}$$

$$l_\mu = \left(1, \frac{rx + ay}{r^2 + a^2}, \frac{ry - ax}{r^2 + a^2}, \frac{z}{r}\right), \tag{2.94}$$

$$r^2 = \frac{1}{2}\left(\rho^2 - a^2\right) + \sqrt{\frac{1}{4}\left(\rho^2 - a^2\right)^2 + a^2 z^2}, \tag{2.95}$$

M is the black hole mass, a its spin parameter and $\rho = \sqrt{x^2 + y^2 + z^2}$.

By comparison with Eq. (2.70) it is easy to identify the metric's ADM components. The lapse is given by [53]

$$N = \frac{1}{\sqrt{1 + 2H}}, \tag{2.96}$$

the sift vectors are

$$\beta_i = 2Hl_i \tag{2.97}$$

$$\beta^i = \frac{2H\delta^{ij}l_j}{(1 + 2H)}, \tag{2.98}$$

the 3-metric is

$$\gamma_{ij} = \eta_{ij} + 2Hl_i l_j \tag{2.99}$$

and the extrinsic curvature is

$$K_{ij} = -\partial_t \left(Hl_i l_j\right)/N + 2\left(D_i\left(Hl_j\right) + D_j\left(Hl_i\right)\right) \tag{2.100}$$

where D_i is the covariant derivative associated with γ_{ij}.

We will now summarize the parameter choices made that provide an explicit example of energy extraction. In this example, we have chosen $M = 0.5$ and $a = 0.49$, which is equivalent to 98% of M, a rather large spin parameter,

$E(0)$	m
1.0	1.0×10^{-1}
8.0×10^{-3}	1.0×10^{-4}
$9.199999999999999 \times 10^{-1}$	$9.5800493929138735 \times 10^{-3}$

Table 2.7: Initial energy and masses for the particles participating in the Penrose process example. The first two rows are given explicitly via configuration value and represent the ingoing and Penrose trajectories, respectively. The third row represents the exit trajectory and is computes via conservation of 4-momentum.

chosen to facilitate the process of finding suitable orbits. The break-up point was chosen at coordinates $X^i = (1, 0, 0)$ and the background sphere radius was chosen to be 1.0×10^6. Table 2.7 summarizes the initial energy and mass of the participating particles. The first, second and third rows contain data relative to the entry, Penrose and exit orbits, respectively. The parameters for the entry and Penrose orbits are chosen explicitly via configuration file fed to the code, while the parameters of the exit orbit are computed via the conservation of 4-momentum at the break-point. Note that the masses are explicitly chosen in order to satisfy Eq. (2.45) and to provide a way of computing initial velocities via Eqs. (2.90)-(2.91)

Table 2.8 summarize the initial velocities of the participating particles. Here, the values of the first two rows (representing the ingoing and Penrose trajectories, respectively), were computed via the parametrization described in the previous section together with data from Tab. 2.7 while data on the third row, representing the outgoing particle, was computed via conservation of 4-momentum. The third column in this table shows the value of the ellipse parameter chosen for each orbit (except the exit orbit).

Table 2.9 summarizes the two energy measures (local and global on the first and second column, respectively) at the time when they hit the background sphere. The first row contains data relative to the ingoing orbit while the second contains data relative to the outgoing orbit. Note that t_f does not necessarily coincide for the two orbits, since they might take arbitrarily long paths before escaping to infinity. The third column shows the absolute difference between global and local energies at the background sphere.

$V^x(0)$	$V^y(0)$	Θ
0.6769503786998466	0.6740022058848380	$-25/200\pi$
0.5948571400034293	-0.3343724878526367	$-100/200\pi$
0.67761242094739838	0.68213425986659171	—

Table 2.8: Initial velocities for the particles participating in the Penrose process example. The first two rows are computed using the ellipse parametrization described in the previous section with data provided in Tab. 2.7 together with the parameter provided in the third column and represent the ingoing and Penrose trajectories, respectively. The third row represents the exit trajectory and is computes via conservation of 4-momentum.

$E(t_f)$	$\varepsilon(t_f)$	$|E(t_f) - \varepsilon(t_f)|$
$3.8435595988010596 \times 10^{-1}$	$3.8435613882134312 \times 10^{-1}$	$1.7894123710560095 \times 10^{-7}$
$3.8515962539170862 \times 10^{-1}$	$3.8515904777176790 \times 10^{-1}$	$5.776199407114824 \times 10^{-7}$

Table 2.9: Energy measures at the time of collision with the background sphere. The first and second row represent the ingoing and the outgoing orbits, respectively. The third column shows the absolute difference between energy measures at the background sphere radius. Note that t_f is not necessarily the same for both trajectories.

$E_{\text{out}}(t_f) - E_{\text{in}}(t_f)$	0.0008036655116026026
$\varepsilon_{\text{out}}(t_f) - \varepsilon_{\text{in}}(t_f)$	0.0008029089504247855
η_E	0.0020909406786700896
η_ε	0.0020889722919224165

Table 2.10: Energy difference and extraction efficiency of the process given different energy measures.

Finally, Table 2.10 summarizes the amount of energy extracted from the process in different forms. The first and second rows compute the difference between the energy of the outgoing and ingoing particles using different energy measures (local and global respectively). Since this difference is positive, we can conclude that energy was indeed extracted from the black hole. The last two rows compute the efficiency of the process for the two available energy measures. The efficiency of the process for a given energy measure ϵ is given by

$$\eta_\epsilon = \frac{\epsilon_{\text{out}}(t_f) - \epsilon_{\text{in}}(t_f)}{\epsilon_{\text{in}}(t_f)}. \tag{2.101}$$

Even tough the parameters chose in this example lead to a tiny amount of energy being extracted from the system with a low overall efficiency, we consider it to be a success as a whole: It works as a proof of concept and demonstrates how the proposed framework can be used for studying the Penrose process in a broader context than what was known up until now.

2.5.5 SKS Metric

In this section we will further illustrate our framework by considering a different spacetime metric approximating an astrophysical binary black hole system referred to as the Superimposed Kerr-Schild solution, or SKS solution. The idea behind its construction is rather simple: One simply adds two Kerr solutions in Kerr-Schild coordinates and subtracts from this a Minkowski metric. After that, the black hole terms are further boosted and transformed in order to add motion to the individual black holes. This, of course, does not constitute in an exact solution of Einstein's field equations, nevertheless it can

still be a valuable model for describing astrophysical binaries under certain conditions. The construction and motivation for using this approximation is extensively discussed in Refs. [54, 55], where it was used in numerical simulations of accretion disks around BH binaries. Ref [54], in particular, discusses the success of using superimposed solutions for computing initial data for numerical simulations of black hole mergers and shows that the expansion of the superimposed metric agrees with the lowest Post-Newtonian expansion of the metric of spinning binaries. Furthermore, Ref. [55] compares the superimposed metric with other approximate solutions to binary black holes constructed with a much more mathematically involved technique called "asymptotic matching", that combines Post-Newtonian and other types of solutions in different regions of the spacetime and matches them together into a single solution. It shows that the violations of the Einstein field equations for the models constructed by matching and superposition are very similar in their order of magnitude and profile, with the matching solutions being more well-behaved and smooth at larger distances from the binary black holes. This leads them to conclude that given the mathematical simplicity of constructing a superimposed solution, they are more advantageous to matching solutions from a computational perspective.

Our construction of the SKS metric follows closely Refs. [54, 55], but we shall summarize the procedure here for the sake of clarity. We start by considering two Kerr metrics in Kerr-Schild coordinates $(T^{(i)}, X^{(i)}, Y^{(i)}, Z^{(i)})$ that describe each black hole, labeled by the index $(i) = 1, 2$ and characterized by their masses $M^{(i)}$ and spin parameter $a^{(i)}$ in their rest frame. Let us now suppose there exists a global coordinate frame labeled by coordinates (t, x, y, z) where the constituent black holes follow trajectories $s^{(i)\mu}(t, x, y, z)$. Following Ref. [54], we will consider that the black holes follow a Keplerian orbit, given by

$$s^{(i)\mu} = \left((-1)^{i+1} \frac{b}{2} \cos \Omega t, \ (-1)^{i+1} \frac{b}{2} \sin \Omega t, \ 0 \right), \tag{2.102}$$

where

$$\Omega = \sqrt{\frac{M^{(1)} + M^{(2)}}{b^3}} \tag{2.103}$$

is the orbital angular velocity of the system and b is the coordinate distance (in global coordinates) between the two black hole origins. From Eq. (2.102), we can compute the black hole velocity vector $v^{(i)\mu} = \mathrm{d}s^{(i)\mu}/\mathrm{d}t$ and obtain

$$v^{(i)\mu} = \left((-1)^i \frac{b\Omega}{2} \sin \Omega t, \ (-1)^{i+1} \frac{b\Omega}{2} \cos \Omega t, \ 0 \right), \tag{2.104}$$

which can be normalized to yield

$$n^{(i)\mu} = \left((-1)^i \sin \Omega t, \ (-1)^{i+1} \cos \Omega t, \ 0 \right) \tag{2.105}$$

with norm

$$v^2 \equiv \sum_{\mu=0}^{2} v^{(i)\mu} = \frac{b^2 \Omega^2}{4}. \tag{2.106}$$

With these quantities, we can see that the Lorentz factor, γ, is given by

$$\gamma \equiv \frac{1}{\sqrt{1 - v^2}} = \frac{2}{\sqrt{4 - b^2 \Omega^2}}. \tag{2.107}$$

It's then trivial to compute the generalized Lorentz boost of the trajectories

$$\Lambda^{(i)\mu}{}_{\nu} = \begin{pmatrix} \gamma & -\gamma v^{(i)0} & -\gamma v^{(i)1} & 0 \\ -\gamma v^{(i)0} & 1 + (\gamma - 1)n^{(i)0}n^{(i)0} & (\gamma - 1)n^{(i)0}n^{(i)1} & 0 \\ -\gamma v^{(i)1} & (\gamma - 1)n^{(i)1}n^{(i)0} & 1 + (\gamma - 1)n^{(i)1}n^{(i)1} & 0 \\ 0 & 0 & 0 & 1 \end{pmatrix} \tag{2.108}$$

by virtue of Eqs. (2.104)-(2.107). The next step of the construction, is therefore, to boost each individual Kerr metric using Eq. (2.108). We remind the reader that the Kerr-Schild form of the metric is maintained after a Lorentz boost. Finally, we must transform each local coordinate of each individual black hole to global coordinates. This is done via a non-linear coordinate transformation

(or a "circular boost", as Ref. [54] puts it) that reads

$$t = \gamma \left(T - v^{(i)0}X - v^{(i)1}Y \right) \tag{2.109}$$

$$x = s^{(i)0} + X\left[1 + (\gamma - 1)\, n^{(i)0}n^{(i)0}\right] + Y\left[(\gamma - 1)\, n^{(i)0}n^{(i)1}\right] \tag{2.110}$$

$$y = s^{(i)1} + X\left[(\gamma - 1)\, n^{(i)0}n^{(i)1}\right] + Y\left[1 + (\gamma - 1)\, n^{(i)1}n^{(i)1}\right] \tag{2.111}$$

$$z = Z \tag{2.112}$$

To summarize, the algorithm one must employ in order to construct the SKS metric in global coordinates (t, x, y, z) with black holes that are following the Keplerian trajectories given by Eq. (2.102) and possess mass and spin parameters $M^{(1,2)}$ and $a^{(1,2)}$, respectively, and coordinate separation b is as follows:

1. Compute the value of Ω from the metric parameters (masses and separation) via Eq. (2.103).

2. Using the previous step, compute γ via Eq. (2.107).

3. Compute each component of the trajectory velocity vector $v^{(i)\mu}$ and normal vector $n^{(i)\mu}$ via Eqs. (2.104) and (2.105), respectively.

4. Construct the Lorentz boost matrix via Eq. (2.108).

5. Boost the "black hole part" of the Kerr-Schild metric, that is, replace $M_{\mu\nu} = Hl_\mu l_\nu$ by $\overline{M}_{\mu\nu}^{(i)} = H^{(i)}\Lambda^{(i)\alpha}{}_\mu \Lambda^{(i)\beta}{}_\nu l_\alpha^{(i)} l_\beta^{(i)}$ for each black hole.

6. Find the coordinate values $(T^{(i)}, X^{(i)}, Y^{(i)}, Z^{(i)})$ for each black hole by inverting the system formed by Eqs. (2.109)-(2.112).

7. Substitute $(T^{(i)}, X^{(i)}, Y^{(i)}, Z^{(i)})$ into $\overline{M}_{\mu\nu}^{(i)}$, producing $\overline{\mathcal{H}}_{\mu\nu}^{(i)}(t, x, y, z)$.

8. The final metric components are given by $g_{\mu\nu}(t, x, y, z) = \eta_{\mu\nu} + \overline{\mathcal{H}}_{\mu\nu}^{(1)} + \overline{\mathcal{H}}_{\mu\nu}^{(2)}$.

We have implemented the SKS solution as a plugin in GRLensing and validated the implementation by comparing plots of the metric components against the results of Ref. [55]. We have also constructed the metric analytically using a Mathematica notebook that was also used in order to independently

check the components as implemented in the C++ code and cross-check those results against Ref. [55]. Furthermore, we have also used this notebook to identify the region where the g_{tt} component changes its sign. This region can be understood as the "ergosphere" viewed by an observer living in the global reference frame labeled by (t, x, y, z). Note however, that strictly speaking the use of the word "ergosphere" in this context is an abuse, since it refers to a region that is globally defined via the existence of the time-like killing vector field. Nevertheless, we can observe this region as the spacetime metric parameters change, similarly to our work in Sections 2.3 and 2.4. The general features of the local ergosphere in the SKS metric resemble that of the CMMR metric, presented in Sec. 2.4, with the remarkable difference that the Lorentz boosts required for the construction of the SKS spacetime make the ergospheres "flattened" the direction of the motion of the holes. This is a well-known effect that can be observed even in the Schwarzschild spacetime, as demonstrated in Ref. [56]. Fig. 2.17 illustrates relevant regions in the SKS spacetime with black holes masses $M^{(1)} = M^{(2)} = 1/2$, spin parameters $a^{(1)} = a^{(2)} = 1/4$ and separation parameter $b = 3$. The boundary of the local ergosphere is marked in red, the approximate location of the event horizons in gray, the singular region in black and the black hole centers are indicated by black crosshairs. As was previously mentioned, the boundary of the ergosphere is marked as the surface where the g_{tt} component changes its sign. The event horizons and singular regions are given by [54]

$$r^{(1,2)} = 2M^{(1,2)} \left(M^{(1,2)} + \sqrt{M^{(1,2)} - \left(a^{(1,2)}\right)^2} \right) \qquad (2.113)$$

and

$$r^{(1,2)} = \left|a^{(1,2)}\right|, \qquad (2.114)$$

respectively, where $r^{(1,2)}$ is the coordinate distance measured from one of the black hole centers. The figure shows that the ergosphere gets "dragged along" the direction of motion of the black holes.
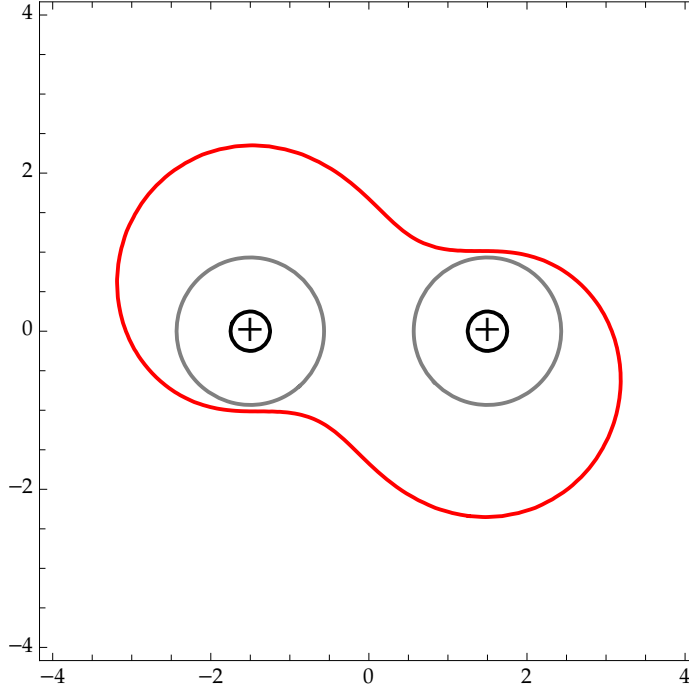
Figure 2.17: Regions of interest in the SKS metric. The red region marks the boundary of the local ergosphere while the gray and black regions mark, respectively, the event horizons and singularities. The black crosshairs mark the centers of the black holes. The spacetimes parameters were chosen to be $M^{(1)} = M^{(2)} = 1/2$, $a^{(1)} = a^{(2)} = 1/4$ and $b = 3$

2.5.5.1 Example 1

For our first example, we have chosen the system parameters as $M^{(1)} = M^{(2)} = 1/2$, $a^{(1)} = a^{(2)} = 0.49$ and $b = 10$. The break-up point was chosen at coordinates $X^i = (6.3, 0, 0)$ and the background sphere radius was chosen to be 1.0×10^6. Following the same template of Table 2.7, Table 2.11 summarizes the initial energy and mass of the participating particles. Once again, the first, second and third rows contain data relative to the entry, Penrose and exit orbits, respectively. The parameters for the entry and Penrose orbits are chosen explicitly via configuration file fed to the code, while the parameters of the exit orbit are computed via the conservation of 4-momentum at the break-point. The masses are explicitly chosen in order to satisfy Eq. (2.45) and to provide a way of computing initial velocities via Eqs. (2.90)-(2.91)

$E(0)$	m
1.0	1.0×10^{-1}
8.0×10^{-3}	1.0×10^{-4}
$9.919999999999999 \times 10^{-1}$	$9.5800493929022838 \times 10^{-3}$

Table 2.11: Initial energy and masses for the particles participating in the Penrose process example. The first two rows are given explicitly via configuration value and represent the ingoing and Penrose trajectories, respectively. The third row represents the exit trajectory and is computes via conservation of 4-momentum.

$V^x(0)$	$V^y(0)$	Θ
0.6769503786998466	0.6740022058848380	$-25/200\pi$
0.5948571400034293	-0.3343724878526367	$-100/200\pi$
0.66011565390809868	0.68380243736284951	—

Table 2.12: Initial velocities for the particles participating in the Penrose process example. The first two rows are computed using the ellipse parametrization described in the previous section with data provided in Tab. 2.11 together with the parameter provided in the third column and represent the ingoing and Penrose trajectories, respectively. The third row represents the exit trajectory and is computes via conservation of 4-momentum.

Once more, following Table 2.8, Table 2.12 summarizes the initial velocities of the participating particles. Here, the values of the first two rows (representing the ingoing and Penrose trajectories, respectively), were computed via the parametrization described in the previous section together with data from Tab. 2.7 while data on the third row, representing the outgoing particle, was computed via conservation of 4-momentum. The third column in this table shows the value of the ellipse parameter chosen for each orbit (except the exit orbit).

As Table 2.9, Table 2.13 summarizes the two energy measures (local and global on the first and second column, respectively) at the time when they hit the background sphere. The first row contains data relative to the ingoing orbit while the second contains data relative to the outgoing orbit. Note that t_f does not necessarily coincide for the two orbits, since they might take arbitrarily

$E(t_f)$	$\varepsilon(t_f)$	$|E(t_f) - \varepsilon(t_f)|$
$2.4452985315377770 \times 10^{-1}$	$2.4453006741751246 \times 10^{-1}$	$2.1426373481014949 \times 10^{-7}$
$3.4638508542318119 \times 10^{-1}$	$3.463840057243497 \times 10^{-1}$	$1.0796988314520917 \times 10^{-6}$

Table 2.13: Energy measures at the time of collision with the background sphere. The first and second row represent the ingoing and the outgoing orbits, respectively. The third column shows the absolute difference between energy measures at the background sphere radius. Note that t_f is not necessarily the same for both trajectories.

$E_{\text{out}}(t_f) - E_{\text{in}}(t_f)$	0.10185523226940352
$\varepsilon_{\text{out}}(t_f) - \varepsilon_{\text{in}}(t_f)$	0.10185393830683726
η_E	0.41653495863897544
η_ε	0.41652966700464295

Table 2.14: Energy difference and extraction efficiency of the process given different energy measures.

long paths before escaping to infinity. The third column shows the absolute difference between global and local energies at the background sphere.

Finally, following Table 2.10, Table 2.14 summarizes the amount of energy extracted from the process in different forms. The first and second rows compute the difference between the energy of the outgoing and ingoing particles using different energy measures (local and global respectively). Since this difference is positive, we can conclude that energy was indeed extracted from the black hole. The last two rows compute the efficiency of the process for the two available energy measures, given by Eq (2.101).

2.5.5.2 Example 2

In this example, we repeat the run detailed in Sec. 2.5.5.1 while changing the distance parameter from $b = 10.0$ to $b = 7.21$. We have also changed the break-up point coordinates in each run so that it remains at 1.3 coordinate distance units to the right of the right-most black hole. The results of this variation are summarized in Table 2.15 where it is possible to see that the efficiency decreases as the black wholes get more distant from each other.

d	η_E	η_ε
10.0	0.4165349586389754	0.4165293020302941
9.69	0.4099912589653710	0.4099855399919209
9.38	0.4042822480170929	0.4042767439403118
9.07	0.3994849072973370	0.3994792027270561
8.76	0.3954568832639254	0.3954513766173146
8.45	0.3915618006432178	0.3915564144708418
8.14	0.3857189791093659	0.3857135001267253
7.83	0.3709406424619314	0.3709350873643125
7.52	0.3205512719659607	0.3205458837844264
7.21	0.1207168410527975	0.1207122709189437

Table 2.15: Energy extraction efficiency for the configuration detailed in Sec 2.5.5.1 while varying the distance parameter b and keeping the break-up point at 1.3 coordinate distance unites to the right of the rightmost black hole.

2.5.5.3 Example 3

In this example we vary the mass of the left-most black hole $M^{(2)}$ from 0.5 to 0.275 while also changing the spin parameter according to $a^{(2)} = 0.98M^{(2)}$. We keep fixed the mass $M^{(1)} = 0.5$, the spin parameter $a^{(1)} = 0.49$, the distance parameter $b = 20.0$ and the break-up point $(11.0, 0.0, 0.0)$. This configuration is analogue to that of the single Kerr black hole example of Sec. 2.5.4. The results are summarized in Table 2.16, where it is possible to see that as the mass of the companion black hole decreases, the extraction efficiency decreases.

$M2$	η_E	η_ε
0.500	0.1057279994029897	0.1057236710602922
0.475	0.0870377969920106	0.0870336429442202
0.450	0.0712047949044382	0.0712008663973118
0.425	0.0578255784926676	0.0578218053066227
0.400	0.0465203386664686	0.0465166569217887
0.375	0.0369572283763885	0.0369537431441037
0.350	0.0288551456052595	0.0288518045002344
0.325	0.0219792546154663	0.0219759777138235
0.300	0.0161341223097530	0.0161310745614111
0.275	0.0111575173287062	0.0111545996429916

Table 2.16: Energy extraction efficiency for fixed mass $M^{(1)} = 0.5$, spin parameter $a^{(1)} = 0.49$, distance parameter $b = 20.0$ and break-up point $(11.0, 0.0, 0.0)$ and varying Mass $M^{(2)}$ and spin parameter $a^{(2)} = 0.98M^{(2)}$.

Chapter 3

Quasinormal Modes and the Asymptotic Iteration Method

3.1 Chapter Introduction

When a closed physical system (like a guitar string) is perturbed, it relaxes by emitting certain natural frequencies know as *normal modes*. If, however, the system is open (and therefore energy is being somehow dissipated away), its emitted natural frequencies will decay with time (like for instance sounding a bell in a church). These decaying modes are called *quasinormal modes* (QNMs). Such frequencies can be used to obtain information about the system that produces them and black holes, like church bells, are also subject to these phenomena: Perturbed black holes relax by emitting waves in characteristic frequencies that decay with time, thanks to the dissipative nature of the event horizon. See Refs. [57, 58, 59, 60] for an in-depth review of the quasinormal mode problem in the context of general relativity and black holes. Determining these characteristic frequencies quickly and accurately for a large range of models is important for many practical reasons. It has been shown that the gravitational wave signal emitted at the final stage of the coalescence of two compact objects is well described by quasinormal modes [61, 62]. This means that if one has access to a database of quasinormal modes and of gravitational wave signals from astrophysical collision events, it is possible to characterize

the remnant object using its quasinormal frequencies. Since there are many models that aim to describe remnants, being able to compute the quasinormal frequencies for such models reliably is paramount for confirming or discarding them. Very often, computing quasinormal modes reduces to finding the discrete eigenvalue set of a second order differential equation with appropriate boundary conditions and asymptotic behavior. In this chapter, we will explore a numerical technique recently developed for tackling this problem, known as the *Asymptotic Iteration Method* (AIM). The groundwork of the technique was laid out in Ref. [63] and in Ref. [64] the method was refined and adapted to GR.

Motivated by these developments, we have implemented `QuasinormalModes.jl` (see the acompanying paper in Ref. [65]), a `Julia` [66] software package for finding quasinormal modes using the AIM. Not only that, the package can be used to compute the discrete eigenvalues of *any* second order homogeneous ODE (such as the energy eigenstates of the time independent Schrödinger equation) provided that these eigenvalues actually exist. The package features a flexible and user-friendly API where the user simply needs to provide the coefficients of the problem ODE after incorporating boundary and asymptotic conditions on it. The user can also choose to use machine or arbitrary precision arithmetic for the underlying floating point operations involved and whether to do computations sequentially or in parallel using threads. The API also tries not to force any particular workflow on the users so that they can incorporate and adapt the existing functionality on their research pipelines without unwanted intrusions. Often user-friendliness, flexibility and performance are treated as mutually exclusive, particularly in scientific applications. By using `Julia` as an implementation language, the package can have all these features simultaneously. Another important motivation for using `Julia` and writing this package was the lack of generalist, free (both in the financial and license-wise sense) open source tools that serve the same purpose. More precisely, there are tools which are free and open source, but run on top of a proprietary paid and expensive software framework such as the ones developed in Refs. [67, 68], which are both excellent packages that aim to perform the same task as `QuasinormalModes.jl` and can be obtained

and modified freely but, unfortunately, require the user to own a license of the proprietary `Wolfram Mathematica` CAS. Furthermore, their implementations are limited to solve problems where the eigenvalues must appear in the ODE as polynomials of order p. While this is not prohibitively restrictive to most astrophysics problems, it can be an important limitation in other areas. There are also packages that are free and run on top of `Mathematica` but are not aimed at being general eigenvalue solvers at all, such as the one in Ref. [69], that can only compute modes of Schwarzschild and Kerr black holes. Finally, the `Python` package in Ref. [70] is open source and free but can only compute Kerr quasinormal modes. `QuasinormalModes.jl` fills the existing gap for free, open source tools that are able to compute discrete eigenvalues (and in particular, quasinormal modes) efficiently for a broad class of models and problems. The package was used in Ref. [71] where non-scalar perturbations were considered. Novel frequencies were obtained and results were compared against literature values, when possible, while also cross-checking results for the same models obtained via the more traditional pseudo-spectral method.

3.2 The asymptotic iteration method

Here we shall briefly review the mathematical foundations of the AIM following closely Ref. [63]. Let us suppose that exists a variable $x \in [a, b]$ where $a, b \in \mathbb{R}$ and functions $\lambda_i = \lambda_i(x) \in \mathbb{R}$ and $s_j = s_i(x) \in \mathbb{R}$ with integer indexes i and j that are $C_\infty(a, b)$. Let us also suppose that there is a function $y = y(x) \in \mathbb{R}$ that satisfies

$$y^{(2)}(x) - \lambda_0(x)y^{(1)}(x) - s_0(x)y(x) = 0 \qquad (3.1)$$

where the parenthesized superscript denotes n derivatives with respect to the variable x. These equations can be found in many areas of physics, such as the time-independent Schrödinger equation in Quantum Mechanics, or the differential equations governing the perturbations of a Schwarzschild black hole. The AIM is based upon the following theorem:

Theorem 3.2.1. *The differential equation* (3.1) *has a general solution of the form*

$$y(x) = \exp\left(-\int^x \alpha \, dt\right)\left\{C_2 + C_1 \int^x \exp\left[\int^t (\lambda_0(\tau) + 2\alpha(\tau)) d\tau\right] dt\right\} \quad (3.2)$$

if for some $n > 0$ the condition

$$\alpha(x) \equiv \frac{s_n(x)}{\lambda_n(x)} = \frac{s_{n-1}(x)}{\lambda_{n-1}(x)} \quad (3.3)$$

or equivalently

$$\delta(x) \equiv s_n(x)\lambda_{n-1}(x) - \lambda_n(x)s_{n-1}(x) = 0 \quad (3.4)$$

is satisfied, where

$$\lambda_k(x) \equiv \lambda_{k-1}^{(1)}(x) + s_{k-1}(x) + \lambda_0(x)\lambda_{k-1}(x) \quad (3.5)$$

$$s_k(x) \equiv s_{k-1}^{(1)}(x) + s_0(x)\lambda_{k-1}(x) \quad (3.6)$$

with $k \in [1, n]$

From now on, we shall refer to the condition expressed by Eq. (3.4) as the *AIM quantization condition*. Provided that Theo. 3.2.1 is satisfied we can find both the eigenvalues and eigenvectors of Eq. (3.1) using, respectively, Eq. (3.4) and Eq. (3.2). More specifically, the quasinormal modes of a perturbed black hole will be the complex frequency values ω that satisfy Eq. (3.4) for any value of x. Recently, it was shown in Ref. [72] that for the method to converge, one must have

$$\lim_{n \to \infty} \frac{\delta_n(x)}{\lambda_{n-1}^2(x)} = 0 \quad (3.7)$$

Despite being quite general, the method presents a computational difficulty hidden in Eq. (3.5) and Eq. (3.6). The definitions of the n-th coefficients are coupled, recursive and involve the derivatives of previous entries. This means that to compute the quantization condition, Eq. (3.4), using n iterations we end up computing the n-th derivatives of λ_0 and s_0 multiple times. Depending on the size of the original functions, the size and complexity of each coefficient can quickly spiral out of control as n is increased. To address these issues, Cho et al. have proposed in Ref. [64] to instead of computing these coefficients directly,

use a Taylor expansion of both $\lambda_n(x)$ and $s_n(x)$ around an arbitrary point ξ where the AIM is to be performed, thus introducing a new free parameter to the method. We, however, remind the reader that the results must be independent of the choice of ξ. Mathematically, we have

$$\lambda_n(\xi) = \sum_{i=0}^{\infty} c_n^i (x - \xi)^i, \tag{3.8}$$

$$s_n(\xi) = \sum_{i=0}^{\infty} d_n^i (x - \xi)^i, \tag{3.9}$$

where c_n^i and d_n^i are the Taylor coefficients of the expansions of λ_n and s_n around ξ, respectively. By plugging Eqs. (3.8) and (3.9) into Eqs. (3.5) and Eq. (3.6) one gets

$$c_n^i = (i+1)c_{n-1}^{i+1} + d_{n-1}^i + \sum_{k=0}^{i} c_0^k c_{n-1}^{i-k}, \tag{3.10}$$

$$d_n^i = (i+1)d_{n-1}^{i+1} + \sum_{k=0}^{i} d_0^k c_{n-1}^{i-k}. \tag{3.11}$$

Finally, using Eqs. (3.10) and (3.11) the quantization condition, Eq. (3.4), becomes

$$\delta \equiv d_n^0 c_{n-1}^0 - d_{n-1}^0 c_n^0 = 0. \tag{3.12}$$

In order to better visualize and understand the improved algorithm, it is useful to arrange the c_n^i (or d_n^i) coefficients as elements of a matrix C (or D), where the index i indicates the matrix row and the index n represents the matrix column. To aid in our visualization, let us also assume, without loss of generality, that we have chose to perform the AIM with $n = 2$. According to Eq. (3.12), the largest n coefficients that need to be computed are d_2^0 and c_2^0. These coefficients need, in turn, to be computed recursively via Eqs. (3.10) and (3.11). This process was represented in Fig. 3.1 for c_2^0. Each row in the figure represents a step in the algorithm. A red circle marks the coefficient that is being calculated at the given step and a blue circle with arrows mark the coefficients that are necessary for the calculation. We remind that the first column of the

matrices, that is, c_0^i and d_0^i, are computed directly from $\lambda_0(x)$ and $s_0(x)$ from their Taylor expansions. Note that the lower right coefficients of the c_n^i matrix, that is, c_1^1, c_2^2 and c_1^2 are never used in any step. Since these coefficients are not required, they need not be computed, saving time in the algorithm.
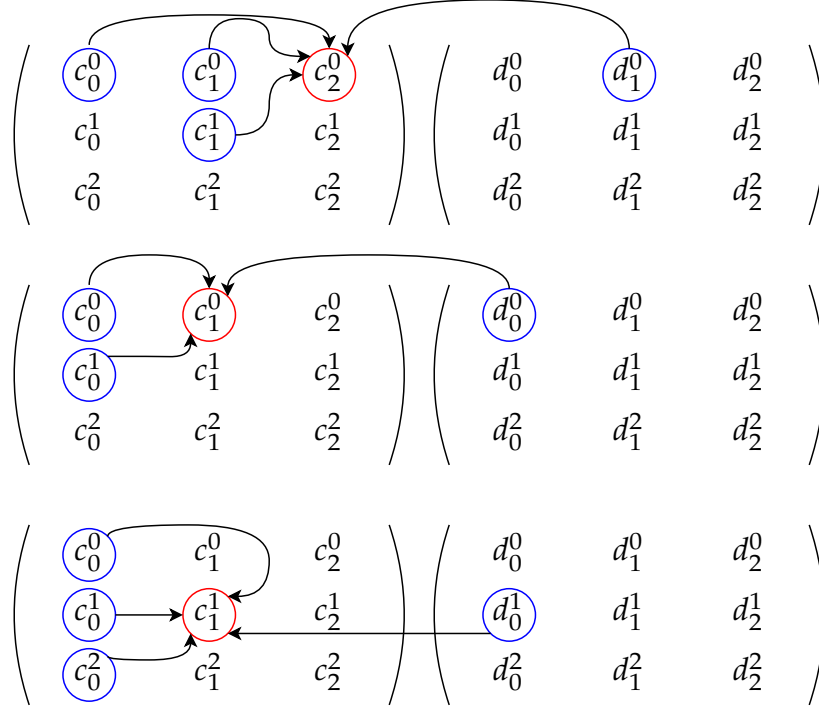

Figure 3.1: Schematic representation of the AIM for computing the c_n^i matrix. Each row of matrices represent an AIM step. Coefficients circled in red are currently being computed, while coefficients marked in blue withe arrows are the coefficients required for that computation. Notice how the lower-right triangle of coefficients is never used.

In Fig. 3.2, we see a similar representation, but now for the d_n^i coefficients. The first two rows of the image represent the steps required for computing d_2^0. Notice however, that d_1^0 (the third row in the image) is not explicitly required for the computation of the target coefficients, but it is required for the computation of c_2^0 and can be readily calculated since it depends only on the initial Taylor expansion of the ODE coefficients. Similarly, coefficients d_2^1, d_2^2 and d_1^2 are never used and thus do not need to be computed.

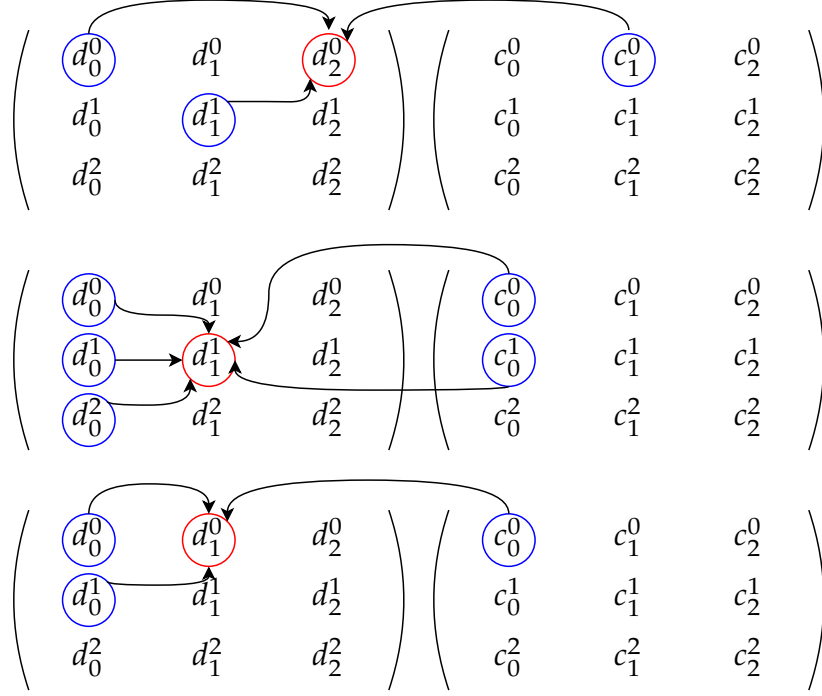These observations motivate us to see the AIM algorithm as an "evolution"

Figure 3.2: Schematic representation of the AIM for computing the d_n^i matrix. The first two row of matrices represent AIM steps and the third row represents the computation of d_1^o, which is required in computing c_2^0. Coefficients circled in red are currently being computed, while coefficients marked in blue withe arrows are the coefficients required for that computation. Notice how the lower-right triangle of coefficients is never used.

of the initial coefficient sets c_0^i and d_0^i by rewriting Eqs. (3.10) and (3.11) as

$$c_{n+1}^i = (i+1)c_n^{i+1} + d_n^i + \sum_{k=0}^{i} c_0^k c_n^{i-k}, \tag{3.13}$$

$$d_{n+1}^i = (i+1)d_n^{i+1} + \sum_{k=0}^{i} d_0^k c_n^{i-k}, . \tag{3.14}$$

We can now devise an algorithm that performs n iterations of the AIM:

1. Construct two arrays of size n where the i-th element is c_0^i (or d_0^i) where i ranges from zero to n. We shall call these `icda` (initial c data array) and `idda` (initial d data array).

2. Construct two arrays of size n to contain the current column of c (or d)

indexes. We shall call these `ccda` (current c data array) and `cdda` (current d data array)

3. Construct two arrays of size n to contain the previous column of c (or d) indexes. We shall call these `pcda` (previous c data array) and `pdda` (previous d data array).

4. Initialize `ccda` with data from `icda` and `cdda` with data from `idda`.

5. Perform n AIM steps using the evolution Eqs. (3.13) and (3.14). That is, repeat the following n times:

    (a) Copy the content from `ccda` into `pcda`

    (b) Copy the content from `cdda` into `pdda`

    (c) Rewrite each element of `ccda` and `cdda` using Eqs. (3.13) and (3.14), respectively.

6. Compute the quantization condition, Eq. (3.12), using the first indexes of each array. Explicitly, perform `cdda[1]*pcda[1] - pdda[1]*ccda[1]`[1].

7. If the coefficients are analytic, determine the roots of the resulting expression, otherwise use steps 1-6 to build a function that returns δ numerically with a given parameter set and use a numerical root finding method to find the roots of this function.

The algorithm steps are depicted in Fig. 4.1 for the $n = 2$ example. Each array is depicted as a sequence of blue (for storing c_n^i coefficient) and red (for storing d_n^i coefficients) squares, wherein each square is an array element. There are three columns of arrays, each representing, respectively, initial, current and previous data at various points in the algorithm. Each row indicates the algorithmic step that it represents to the left of the data arrays and which AIM step (n value) a set of steps corresponds to. On step 5 (c), colored arrows indicate the data dependency of each index in the current arrays (similarly to what is depicted in Figs. 3.1 and 3.2). Hatches in array indexes represent data that is not evolved/computed.

---

[1]We assume 1-base array indexing, the same scheme adopted by the `Julia`.
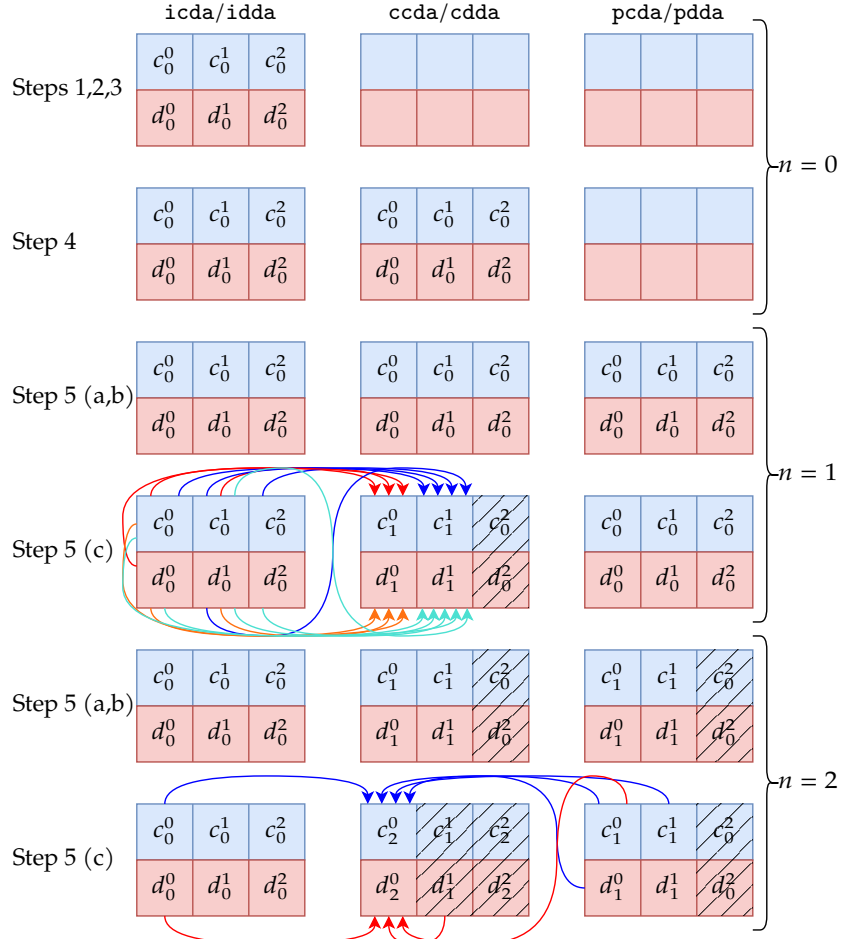
Figure 3.3: Representation of AIM steps for an $n = 2$ sized example. Arrays are represented by a sequence of blue (for storing c_n^i coefficient) and red (for storing d_n^i coefficients) squares, wherein each square is an array element. Each column represents, respectively, initial, current and previous data. Colored arrows indicate index dependencies. Hatches indicate ignored data.

3.3 QuasinormalModes.jl

We will now describe results obtained with `QuasinormalModes.jl`. We will not describe package usage since that topic is covered in details in the extensive package documentation, available online here. The code is hosted on GitHub and can be found in Ref. [73]. The package is registered in the `Julia` package index and can be easily installed with instructions provided in the `README` of the

GitHub repository.

3.3.1 Convergence and benchmarking

We have written a script to test the package's performance and convergence characteristics. The script computes the fundamental $s = l = 0$ mode of a Schwarzschild black hole while sweeping the number of AIM iterations from $n = 1$ to $n = 100$. The error of the computation as well as the time taken to compute the result and the number of iterations performed is repeated 20 times and each run is saved to a different text file in order to increase the statistical significance of the time measurements. The error measure is defined as the difference between AIM computed value and values obtained in Ref. [74] via Leaver's continued fraction method. The error convergence results are plotted in Figs. 3.4 using a logarithmic scale in the y axis for both the real (black dots) and imaginary (red crosses) parts of the mode a function the number of AIM iterations performed. It is possible to observe, despite oscillations, an overall trend of convergence towards the reference values. The (20 repetitions) average time taken as a function of the number of iterations is presented in Fig. 3.5 in a log-log plot. It is possible to see that the time taken increases with a power law trend as the number of AIM iterations gets higher.

3.3.2 Comparison with pseudo-spectral methods

We have, with collaborators in Ref. [71], revisited the problem of computing QNMs resulting from perturbations of spins 0, 1/2, 1, 3/2, 2, 5/2 of an asymptotically flat Schwarzschild black hole. Our aim was to compare numerical results obtained via the AIM with those obtained using the pseudo-spectral method and contrast both results with data available in the literature whenever possible. We have computed higher overtones quasinormal frequencies for all the investigated perturbation fields and obtained purely imaginary frequencies for spin 1/2 and 3/2 fields that are in agreement with analytic results reported previously in the literature. The purely imaginary frequencies for the spin 1/2 perturbation field are exactly the same as the frequencies obtained for the spin 3/2 perturbation field. Finally, we computed,
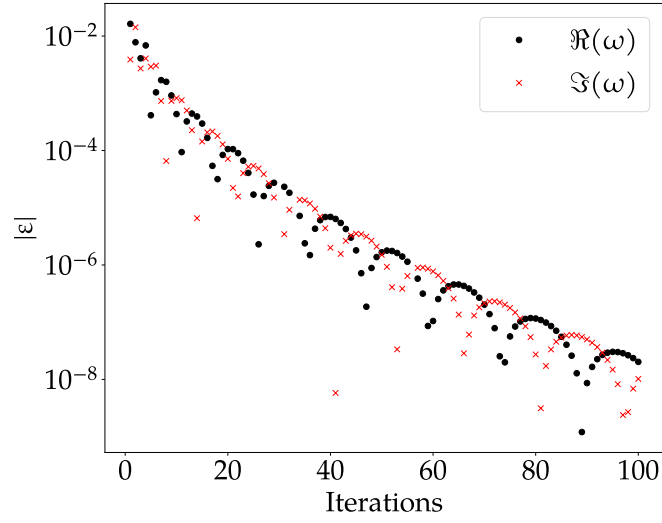
Figure 3.4: Error of the fundamental $s = l = 0$ Schwarzschild QNM vs. the number of AIM iterations. Reference values obtained in Ref. [74]. The y-axis of the plot is in logarithmic scale.

Figure 3.5: Time taken (average of 20 repetitions) vs. the number of AIM iterations taken to compute the fundamental Schwarzschild QNM. The plot is in a log-log scale.

the quasinormal frequencies for the spin 5/2 perturbation field for the very first time, and purely imaginary frequencies are found also in this case.

3.3.2.1 Integer spin results

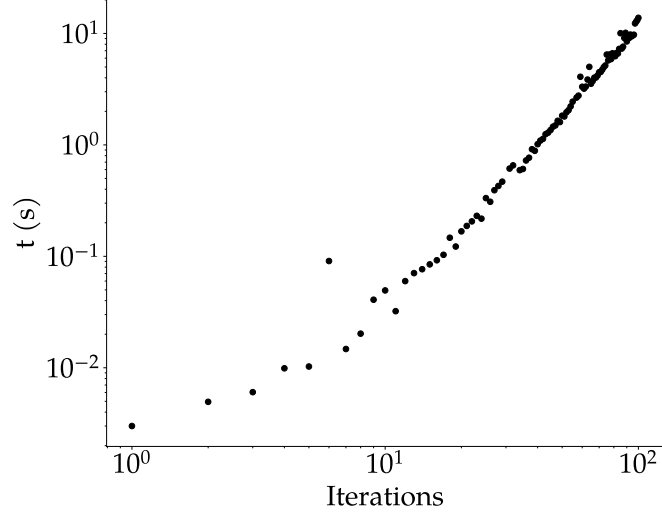| l	n	Pseudo-spectral I (60 Polynomials)	Pseudo-spectral II (40 polynomials)	AIM 100 Iterations	Ref. [75]	Ref. [76]
0	0	$\pm 0.110455 - 0.104896i$	$\pm 0.110455 - 0.104896i$	$\pm 0.110455 - 0.104896i$	$0.1046 - 0.1152i$	$\pm 0.1105 - 0.1008i$
1	0	$\pm 0.292936 - 0.097660i$	$\pm 0.292936 - 0.097660i$	$\pm 0.292936 - 0.097660i$	$0.2911 - 0.0980i$	$\pm 0.2929 - 0.0978i$
	1	$\pm 0.264449 - 0.306257i$	$\pm 0.264449 - 0.306257i$	$\pm 0.264449 - 0.306257i$	—	$\pm 0.2645 - 0.3065i$
2	0	$\pm 0.483644 - 0.096759i$	$\pm 0.483644 - 0.096759i$	$\pm 0.483644 - 0.096759i$	$0.4832 - 0.0968i$	$\pm 0.4836 - 0.0968i$
	1	$\pm 0.463851 - 0.295604i$	$\pm 0.463851 - 0.295604i$	$\pm 0.463851 - 0.295604i$	$0.4632 - 0.2958i$	$\pm 0.4638 - 0.2956i$
	2	$\pm 0.430544 - 0.508558i$	$\pm 0.430544 - 0.508558i$	$\pm 0.430544 - 0.508558i$	—	$\pm 0.4304 - 0.5087i$
3	0	$\pm 0.675366 - 0.096500i$	$\pm 0.675366 - 0.096500i$	$\pm 0.675366 - 0.096500i$	$0.6752 - 0.0965i$	—
	1	$\pm 0.660671 - 0.292285i$	$\pm 0.660671 - 0.292285i$	$\pm 0.660671 - 0.292285i$	$0.6604 - 0.2923i$	—
	2	$\pm 0.633626 - 0.496008i$	$\pm 0.633626 - 0.496008i$	$\pm 0.633626 - 0.496008i$	$0.6348 - 0.4941i$	—
	3	$\pm 0.598773 - 0.711221i$	$\pm 0.598773 - 0.711221i$	$\pm 0.598773 - 0.711221i$	—	—
4	0	$\pm 0.867416 - 0.096392i$	$\pm 0.867416 - 0.096392i$	$\pm 0.867416 - 0.096392i$	$0.8673 - 0.0964i$	—
	1	$\pm 0.855808 - 0.290876i$	$\pm 0.855808 - 0.290876i$	$\pm 0.855808 - 0.290876i$	$0.8557 - 0.2909i$	—
	2	$\pm 0.833692 - 0.490325i$	$\pm 0.833692 - 0.490325i$	$\pm 0.833692 - 0.490325i$	$0.8345 - 0.4895i$	—
	3	$\pm 0.803288 - 0.697482i$	$\pm 0.803288 - 0.697482i$	$\pm 0.803288 - 0.697482i$	$0.8064 - 0.6926i$	—
	4	$\pm 0.767733 - 0.914019i$	$\pm 0.767733 - 0.914019i$	$\pm 0.767733 - 0.914019i$	—	—

Table 3.1: Quasinormal frequencies of the spin 0 perturbations normalized by the mass ($M\omega$) compared against the results of Refs. [75, 76].

3.3.2.2 Semi-integer spin

l	n	Pseudo-spectral I (60 Polynomials)	Pseudo-spectral II (40 polynomials)	AIM 100 Iterations	Ref. [75]	Ref. [76]
1	0	$\pm 0.248263 - 0.092488i$	$\pm 0.248263 - 0.092488i$	$\pm 0.248263 - 0.092488i$	$0.2459 - 0.0931i$	$\pm 0.2482 - 0.0926i$
	1	$\pm 0.214515 - 0.293668i$	$\pm 0.214515 - 0.293667i$	$\pm 0.214515 - 0.293668i$	—	$\pm 0.2143 - 0.2941i$
2	0	$\pm 0.457596 - 0.095004i$	$\pm 0.457595 - 0.095004i$	$\pm 0.457596 - 0.095004i$	$0.4571 - 0.0951i$	$\pm 0.4576 - 0.0950i$
	1	$\pm 0.436542 - 0.290710i$	$\pm 0.436542 - 0.290710i$	$\pm 0.436542 - 0.290710i$	$0.4358 - 0.2910i$	$\pm 0.4365 - 0.2907i$
	2	$\pm 0.401187 - 0.501587i$	$\pm 0.401187 - 0.501587i$	$\pm 0.401187 - 0.501587i$	—	$\pm 0.4009 - 0.5017i$
3	0	$\pm 0.656899 - 0.095616i$	$\pm 0.656899 - 0.095616i$	$\pm 0.656899 - 0.095616i$	$0.6567 - 0.0956i$	$\pm 0.6569 - 0.0956i$
	1	$\pm 0.641737 - 0.289728i$	$\pm 0.641737 - 0.289728i$	$\pm 0.641737 - 0.289728i$	$0.6415 - 0.2898i$	$\pm 0.6417 - 0.2897i$
	2	$\pm 0.613832 - 0.492066i$	$\pm 0.613832 - 0.492066i$	$\pm 0.613832 - 0.492066i$	$0.6151 - 0.4901i$	$\pm 0.6138 - 0.4921i$
	3	$\pm 0.577919 - 0.706331i$	$\pm 0.577919 - 0.706331i$	$\pm 0.577919 - 0.706330i$	—	$\pm 0.5775 - 0.7065i$
4	0	$\pm 0.853095 - 0.095860i$	$\pm 0.853095 - 0.095860i$	$\pm 0.853095 - 0.095810i$	$0.8530 - 0.0959i$	—
	1	$\pm 0.841267 - 0.289315i$	$\pm 0.841267 - 0.289315i$	$\pm 0.841267 - 0.289315i$	$0.8411 - 0.2893i$	—
	2	$\pm 0.818728 - 0.487838i$	$\pm 0.818728 - 0.487838i$	$\pm 0.818728 - 0.487838i$	$0.8196 - 0.4870i$	—
	3	$\pm 0.787748 - 0.694242i$	$\pm 0.787748 - 0.694242i$	$\pm 0.787748 - 0.694242i$	$0.7909 - 0.6892i$	—
	4	$\pm 0.751549 - 0.910242i$	$\pm 0.751549 - 0.910242i$	$\pm 0.751549 - 0.910242i$	—	—

Table 3.2: Quasinormal frequencies of the spin 1 perturbations normalized by the mass ($M\omega$) compared against the results of Refs. [75, 76].

l	n	Pseudo-spectral I (60 Polynomials)	Pseudo-spectral II (40 polynomials)	AIM 100 Iterations	Ref. [75]	Ref. [76]
2	0	$\pm 0.373672 - 0.088962i$	$\pm 0.373672 - 0.088962i$	$\pm 0.373672 - 0.088962i$	$0.3730 - 0.0891i$	$\pm 0.3736 - 0.0890i$
	1	$\pm 0.346711 - 0.273915i$	$\pm 0.346711 - 0.273915i$	$\pm 0.346711 - 0.273915i$	$0.3452 - 0.2746i$	$\pm 0.3463 - 0.2735i$
	2	$\pm 0.301053 - 0.478277i$	$\pm 0.301053 - 0.478277i$	$\pm 0.301053 - 0.478277i$	—	$\pm 0.2985 - 0.4776i$
3	0	$\pm 0.599443 - 0.092703i$	$\pm 0.599443 - 0.092703i$	$\pm 0.599443 - 0.092703i$	$0.5993 - 0.0927i$	$\pm 0.5994 - 0.0927i$
	1	$\pm 0.582644 - 0.281298i$	$\pm 0.582644 - 0.281298i$	$\pm 0.582644 - 0.281298i$	$0.5824 - 0.2814i$	$\pm 0.5826 - 0.2813i$
	2	$\pm 0.551685 - 0.479093i$	$\pm 0.551685 - 0.479093i$	$\pm 0.551685 - 0.479027i$	$0.5532 - 0.4767i$	$\pm 0.5516 - 0.4790i$
	3	$\pm 0.511962 - 0.690337i$	$\pm 0.511962 - 0.690337i$	$\pm 0.511962 - 0.690337i$	—	$\pm 0.5111 - 0.6905i$
4	0	$\pm 0.809178 - 0.094164i$	$\pm 0.809178 - 0.094164i$	$\pm 0.809178 - 0.094164i$	$0.8091 - 0.0942i$	$\pm 0.8092 - 0.0942i$
	1	$\pm 0.796632 - 0.284334i$	$\pm 0.796632 - 0.284334i$	$\pm 0.796632 - 0.284334i$	$0.7965 - 0.2844i$	$\pm 0.7966 - 0.2843i$
	2	$\pm 0.772710 - 0.479908i$	$\pm 0.772710 - 0.479908i$	$\pm 0.772710 - 0.479908i$	$0.7736 - 0.4790i$	$\pm 0.7727 - 0.4799i$
	3	$\pm 0.739837 - 0.683924i$	$\pm 0.739837 - 0.683924i$	$\pm 0.739837 - 0.683924i$	$0.7433 - 0.6783i$	$\pm 0.7397 - 0.6839i$
	4	$\pm 0.701516 - 0.898239i$	$\pm 0.701516 - 0.898239i$	$\pm 0.701516 - 0.898239i$	—	$\pm 0.7006 - 0.8985i$

Table 3.3: Quasinormal frequencies of spin 2 perturbations normalized by the mass ($M\omega$) compared against the results of Refs. [75, 76].

l	n	Pseudo-spectral I (60 Polynomials)	Pseudo-spectral II (40 polynomials)	AIM 100 Iterations	Ref. [75]	Ref. [77]
0	0	$\pm 0.182963 - 0.096982i$	$\pm 0.182963 - 0.096982i$	$\pm 0.182963 - 0.096824i$	—	—
1	0	$\pm 0.380037 - 0.096405i$	$\pm 0.380037 - 0.096405i$	$\pm 0.380037 - 0.096405i$	$0.3786 - 0.0965i$	$0.379 - 0.097i$
	1	$\pm 0.355833 - 0.297497i$	$\pm 0.355833 - 0.297497i$	$\pm 0.355833 - 0.297497i$	—	—
2	0	$\pm 0.574094 - 0.096305i$	$\pm 0.574094 - 0.096305i$	$\pm 0.574094 - 0.096305i$	$0.5737 - 0.0963i$	$0.574 - 0.096i$
	1	$\pm 0.557015 - 0.292715i$	$\pm 0.557015 - 0.292715i$	$\pm 0.557015 - 0.292715i$	$0.5562 - 0.2930i$	$0.556 - 0.293i$
	2	$\pm 0.526607 - 0.499695i$	$\pm 0.526607 - 0.499695i$	$\pm 0.526607 - 0.499695i$	—	—
3	0	$\pm 0.767355 - 0.096270i$	$\pm 0.767355 - 0.096270i$	$\pm 0.767355 - 0.096270i$	$0.7672 - 0.0963i$	$0.767 - 0.096i$
	1	$\pm 0.754300 - 0.290968i$	$\pm 0.754300 - 0.290968i$	$\pm 0.754300 - 0.290968i$	$0.7540 - 0.2910i$	$0.754 - 0.291i$
	2	$\pm 0.729770 - 0.491910i$	$\pm 0.729770 - 0.491910i$	$\pm 0.729770 - 0.491910i$	$0.7304 - 0.4909i$	$0.730 - 0.491i$
	3	$\pm 0.696913 - 0.702293i$	$\pm 0.696913 - 0.702293i$	$\pm 0.696913 - 0.702293i$	—	—
4	0	$\pm 0.960293 - 0.096254i$	$\pm 0.960293 - 0.096254i$	$\pm 0.960293 - 0.096254i$	$0.9602 - 0.0963i$	$0.960 - 0.096i$
	1	$\pm 0.949759 - 0.290148i$	$\pm 0.949759 - 0.290148i$	$\pm 0.949759 - 0.290148i$	$0.9496 - 0.2902i$	$0.950 - 0.290i$
	2	$\pm 0.929494 - 0.488116i$	$\pm 0.929494 - 0.488116i$	$\pm 0.929494 - 0.488116i$	$0.9300 - 0.4876i$	$0.930 - 0.488i$
	3	$\pm 0.901129 - 0.692520i$	$\pm 0.901129 - 0.692520i$	$\pm 0.901129 - 0.692520i$	$0.9036 - 0.6892i$	$0.904 - 0.689i$
	4	$\pm 0.867043 - 0.905047i$	$\pm 0.867008 - 0.905066i$	$\pm 0.867043 - 0.905047i$	—	—

Table 3.4: Quasinormal frequencies of the spin 1/2 perturbations normalized by the mass ($M\omega$) compared against the results of Refs. [77, 75].

Pseudo-spectral I (60 Polynomials)	Pseudo-spectral II (40 polynomials)	AIM 100 Iterations
$-0.250000i$	$-0.250000i$	$-0.250000i$
$-0.500000i$	$-0.500000i$	$-0.500000i$
$-0.750000i$	$-0.750000i$	$-0.750000i$
$-1.000000i$	$-1.000000i$	$-1.000031i$
$-1.2499998i$	$-1.250000i$	$-1.246550i$

Table 3.5: Purely imaginary frequencies for spin 1/2 perturbations normalized by the mass ($M\omega$). The numerical values of such frequencies are exactly the same as for the purely imaginary frequencies arising in the QNM of spin 3/2 perturbations.

l	n	Pseudo-spectral I (60 Polynomials)	Pseudo-spectral II (40 polynomials)	AIM 100 Iterations	Ref. [75]	Ref. [78]
0	0	$\pm 0.311292 - 0.090087i$	$\pm 0.311292 - 0.090087i$	$\pm 0.311292 - 0.090087i$	—	$0.3112 - 0.0902i$
1	0	$\pm 0.530048 - 0.093751i$	$\pm 0.530048 - 0.093751i$	$\pm 0.530048 - 0.093751i$	—	$0.5300 - 0.0937i$
	1	$\pm 0.511392 - 0.285423i$	$\pm 0.511392 - 0.285423i$	$\pm 0.511392 - 0.285423i$	—	$0.5113 - 0.2854i$
2	0	$\pm 0.734750 - 0.094878i$	$\pm 0.734750 - 0.094878i$	$\pm 0.734750 - 0.094878i$	$\pm 0.7346 - 0.0949i$	$0.7347 - 0.0948i$
	1	$\pm 0.721047 - 0.286906i$	$\pm 0.721047 - 0.286906i$	$\pm 0.721047 - 0.286906i$	$\pm 0.7206 - 0.2870i$	$0.7210 - 0.2869i$
	2	$\pm 0.695287 - 0.485524i$	$\pm 0.695287 - 0.485524i$	$\pm 0.695287 - 0.485524i$	—	$0.6952 - 0.4855i$
3	0	$\pm 0.934364 - 0.095376i$	$\pm 0.934364 - 0.095376i$	$\pm 0.934364 - 0.095376i$	$\pm 0.9343 - 0.0954i$	$0.9343 - 0.0953i$
	1	$\pm 0.923502 - 0.287560i$	$\pm 0.923502 - 0.287560i$	$\pm 0.923502 - 0.287560i$	$\pm 0.9233 - 0.2876i$	$0.9235 - 0.2875i$
	2	$\pm 0.902599 - 0.483957i$	$\pm 0.902599 - 0.483957i$	$\pm 0.902599 - 0.483957i$	$\pm 0.9031 - 0.4835i$	$0.9025 - 0.4839i$
	3	$\pm 0.873342 - 0.687024i$	$\pm 0.873343 - 0.687024i$	$\pm 0.873342 - 0.687024i$	—	$0.8732 - 0.6870i$
4	0	$\pm 1.131530 - 0.095640i$	$\pm 1.131530 - 0.095640i$	$\pm 1.131530 - 0.095640i$	$\pm 1.1315 - 0.0956i$	$1.1315 - 0.0956i$
	1	$\pm 1.122523 - 0.287908i$	$\pm 1.122523 - 0.287908i$	$\pm 1.122523 - 0.287908i$	$\pm 1.1224 - 0.2879i$	$1.1225 - 0.2879i$
	2	$\pm 1.104976 - 0.483096i$	$\pm 1.104976 - 0.483096i$	$\pm 1.104976 - 0.483096i$	$\pm 1.1053 - 0.4828i$	$1.1049 - 0.4830i$
	3	$\pm 1.079852 - 0.683000i$	$\pm 1.079852 - 0.683000i$	$\pm 1.079852 - 0.683000i$	$\pm 1.0817 - 0.6812i$	$1.0798 - 0.6829i$
	4	$\pm 1.048599 - 0.889113i$	$\pm 1.048596 - 0.889115i$	$\pm 1.048599 - 0.889113i$	—	$1.0484 - 0.8890i$

Table 3.6: Quasinormal frequencies of spin 3/2 perturbations normalized by the mass ($M\omega$) compared against the results of Refs. [78, 75].

l	n	Pseudo-spectral I (60 Polynomials)	Pseudo-spectral II (40 polynomials)	AIM 100 Iterations
0	0	$\pm 0.462727 - 0.092578i$	$\pm 0.462727 - 0.092578i$	$0.462727 - 0.092577i$
1	0	$\pm 0.687103 - 0.094566i$	$\pm 0.687103 - 0.094566i$	$0.687103 - 0.094566i$
	1	$\pm 0.670542 - 0.285767i$	$\pm 0.670542 - 0.285767i$	$0.670542 - 0.285767i$
2	0	$\pm 0.897345 - 0.095309i$	$\pm 0.897345 - 0.095309i$	$0.897345 - 0.095309i$
	1	$\pm 0.884980 - 0.287266i$	$\pm 0.884980 - 0.287266i$	$0.884980 - 0.287266i$
	2	$\pm 0.861109 - 0.483113i$	$\pm 0.861109 - 0.483113i$	$0.861109 - 0.483113i$
3	0	$\pm 1.101190 - 0.095648i$	$\pm 1.101190 - 0.095648i$	$1.101190 - 0.095648i$
	1	$\pm 1.091300 - 0.287886i$	$\pm 1.091300 - 0.287886i$	$1.091300 - 0.287886i$
	2	$\pm 1.071999 - 0.482895i$	$\pm 1.071999 - 0.482895i$	$1.071999 - 0.482895i$
	3	$\pm 1.044272 - 0.682307i$	$\pm 1.044272 - 0.682307i$	$1.044272 - 0.682307i$
4	0	$\pm 1.301587 - 0.095829i$	$\pm 1.301587 - 0.095829i$	$1.301587 - 0.095829i$
	1	$\pm 1.293328 - 0.288184i$	$\pm 1.293328 - 0.288184i$	$1.293328 - 0.288184i$
	2	$\pm 1.277107 - 0.482604i$	$\pm 1.277107 - 0.482604i$	$1.277107 - 0.482604i$
	3	$\pm 1.253526 - 0.680366i$	$\pm 1.253526 - 0.680366i$	$1.253526 - 0.680366i$
	4	$\pm 1.223513 - 0.882554i$	$\pm 1.223512 - 0.882553i$	$1.223513 - 0.882554i$

Table 3.7: Quasinormal frequencies of spin 5/2 perturbations normalized by the mass ($M\omega$).

Pseudo-spectral I (60 Polynomials)	Pseudo-spectral II (40 polynomials)	AIM 100 Iterations
$-0.125000i$	$-0.125000i$	$-0.125000i$
$-0.375602i$	$-0.375602i$	$-0.378659i$
$-0.626877i$	$-0.626877i$	$-0.623931i$
$-0.878946i$	$-0.878948i$	$-0.907374i$

Table 3.8: Purely imaginary frequencies of spin 5/2 perturbations normalized by the mass ($M\omega$).

Chapter 4

Numerical Scalar Wave Scattering in GW150914

4.1 Chapter Introduction

In this chapter, we will focus on the numerical simulation of a scalar wave scattering off a black hole binary that mirrors the first event detected by LIGO, know as GW150914. Due to the already discussed challenges imposed by the strong gravity and the highly dynamic nature of astrophysical binary systems, to accurately simulate wave scattering around black hole binaries, it is necessary to solve Einstein's field equations numerically. In recent years, significant progress has been made in the numerical simulation of black hole binaries thanks to state-of-the-art strongly hyperbolic reformulations of the field equations, such as the BSSN formulation [79, 80] and advancements in the understanding of stability criteria in partial differential equation discretization schemes employing techniques such as summation by parts [81]. These techniques have enabled us to simulate the dynamics of black hole binaries and their gravitational wave emission with unprecedented accuracy, stability and reliability.

Numerical evolution through self-coding can be a daunting task. This is where the employment of pre-existing tools, such as the `EinsteinToolkit` [82], becomes beneficial. The `EinsteinToolkit` is, according to its home page, "a

community-driven software platform of core computational tools to advance and support research in relativistic astrophysics and gravitational physics.". The `EinsteinToolkit` is composed of a variety of software modules, referred to as `Thorns`, that are integrated into the `Cactus` [83, 84, 85] computational framework. Each `Thorn` has the ability to perform a range of tasks, including infrastructure tasks such as file input/output, adaptive mesh refinement (AMR), as well as physics-related tasks such as the evolution of binary systems, the extraction of gravitational waves, and the multipole decomposition of a signal.

In the following sections, I will introduce the equations utilized for the evolution of a scalar wave atop a numerically metric without back-reaction, where the spacetime evolution disregards the scalar field's contribution to its stress-energy-momentum tensor. Subsequently, I will provide a detailed description of the `EinsteinToolkit Thorn KleinGordon` responsible for this evolution, and present the results that have been obtained thus far. The scalar field evolution code was developed by the author and its available, together with useful resources, in the `GitHub` repository [86]. It is hoped that these results will offer valuable insights into the dynamics of the relaxation of astrophysical binary systems when perturbed.

4.2 Mathematical formulation

4.2.1 Evolution System

The formulation employed in this chapter was initially developed and published in Ref. [87]. Although the primary focus of that publication differs from the subject matter of this chapter, Appendix A of the paper contains the 3+1 decomposed Klein-Gordon equation for a massive scalar field, as presented in equations A3c and A3d. For the sake of completeness, these equations are

$$\partial_t \Phi = -2\alpha K_\phi + \mathcal{L}_\beta \Phi \tag{4.1}$$

$$\partial_t K_\Phi = \alpha \left(K K_\Phi - \frac{1}{2} \gamma^{ij} D_i \partial_j \Phi + \frac{1}{2} \mu^2 \Phi \right) - \frac{1}{2} \gamma^{ij} \partial_i \alpha \partial_j \Phi + \mathcal{L}_\beta K_\Phi, \tag{4.2}$$

where Φ is the scalar field being evolved, K_Φ its "canonical momentum", given by

$$K_\Phi = -\frac{1}{2\alpha}\left(\partial_t - \mathcal{L}_\beta\right)\Phi, \tag{4.3}$$

α is the spacetime lapse, β^i its shift vector, γ^{ij} its induced 3-metric, K the trace of its extrinsic curvature tensor, D_i the covariant derivative associated with γ^{ij}, μ the spacetime mass parameter and $\mathcal{L}_\beta$ is the Lie derivative along the shift vector β^i, given explicitly by

$$\mathcal{L}_\beta\Phi = \beta^i\partial_i\Phi. \tag{4.4}$$

To expand each component of these equations, we utilized the mathematical software package `Wolfram Mathematica`. The resulting expansion was subsequently implemented into the `Thorn` by automatically generating corresponding `C` code from within `Mathematica`. The code used in this process can be found in `Notebooks/equations.nb` of the `Thorn`'s repository.

4.2.2 Initial data

The implementation supports three distinct initial conditions for the scalar field and its canonical momentum. These include a plane wave, an exact Gaussian, and a multipolar Gaussian function. The plane wave and exact Gaussian initial data were developed for the purpose of testing multipatch derivatives in flat spacetime, which will be elaborated on further in subsequent sections. The exact Gaussian initial data is named as such to reflect the fact that it is an exact solution of the Klein-Gordon equation in flat spacetime.

The multipolar Gaussian function is a basic Gaussian function that is multiplied by a linear combination of real spherical harmonics. This particular function was the one chosen during our "production" runs as it has the ability to excite specific modes in the system based on the chosen parameters for the linear combination. The development of this initial data is based on the methodology presented in Ref. [88]. Explicitly, the multipolar Gaussian function M_G is written as

$$M_G(x,y,z) = \sum_{l=0}^{N}\sum_{m=-l}^{l} c_{lm}Y_{lm}(X,Y,Z)G(R - R_0,\sigma) \tag{4.5}$$

where $X = x - x_0$, $Y = y - y0$, $Z = z - z0$, $R = \sqrt{X^2 + Y^2 + Z^2}$, $Y_{lm}(x, y, z)$ are the real spherical harmonics, given by

$$
Y_{lm}(x,y,z) = \begin{cases} (-1)^m \sqrt{\frac{2l+1}{4\pi} \frac{(l-m)!}{(l+m)!}} P_{lm}\left(\frac{z}{\sqrt{x^2+y^2+z^2}}\right) \cos(m \arctan(y,x)) & \text{if } m \geq 0 \\ (-1)^m \sqrt{\frac{2l+1}{4\pi} \frac{(l-|m|)!}{(l+|m|)!}} P_{l|m|}\left(\frac{z}{\sqrt{x^2+y^2+z^2}}\right) \sin(|m| \arctan(y,x)) & \text{if } m < 0 \end{cases}
$$

$$(4.6)$$

$G(r, \sigma)$ is the standard Gaussian function, given by

$$
G(r, \sigma) = \exp\left(-\frac{1}{2}\left(\frac{r}{\sigma}\right)^2\right). \tag{4.7}
$$

The parameters (x_0, y_0, z_0) are the center of the multipolar Gaussian, R_0 its radius and σ the Gaussian width. Once again, code generation routines for the initial data can be found in `Notebooks/equation.nb`
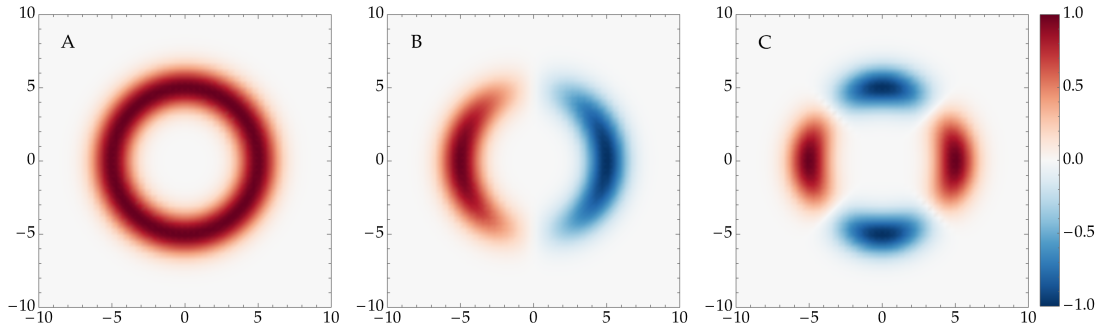

Figure 4.1: TODO.

Chapter 5

Conclusions and perspectives

CONCLUSION

Bibliography

[1] R. A. Hulse and J. H. Taylor, Astrophys. J. **195**, L51 (1975).

[2] B. P. Abbott *et al.* (Virgo, LIGO Scientific), Phys. Rev. Lett. **116**, 061102 (2016), arXiv:1602.03837 [gr-qc] .

[3] E. Berti, APS Physics **9**, 17 (2016), arXiv:1602.04476 [gr-qc] .

[4] M. Visser, in *Kerr Fest: Black Holes in Astrophysics, General Relativity and Quantum Gravity* (2007) arXiv:0706.0622 [gr-qc] .

[5] C. Bambi, Mod. Phys. Lett. A **26**, 2453 (2011), arXiv:1109.4256 [gr-qc] .

[6] S. A. Teukolsky, Class. Quant. Grav. **32**, 124006 (2015), arXiv:1410.2130 [gr-qc] .

[7] E. Berti, Gen. Rel. Grav. **51**, 140 (2019), arXiv:1911.00541 [gr-qc] .

[8] R. Penrose and R. M. Floyd, Nature Physical Science **229**, 177 (1971).

[9] J. D. Schnittman, Gen. Rel. Grav. **50**, 77 (2018), arXiv:1910.02800 [astro-ph.HE] .

[10] S. M. Wagh, S. V. Dhurandhar, and N. Dadhich, The Astrophysical Journal **290**, 12 (1985).

[11] A. Tursunov and N. Dadhich, Universe **5**, 125 (2019), arXiv:1905.05321 [astro-ph.HE] .

[12] A. Tursunov, Z. Stuchlík, M. Kološ, N. Dadhich, and B. Ahmedov, Astrophys. J. **895**, 14 (2020), arXiv:2004.07907 [astro-ph.HE] .

[13] K. Parfrey, A. Philippov, and B. Cerutti, Phys. Rev. Lett. **122**, 035101 (2019), arXiv:1810.03613 [astro-ph.HE] .

[14] S. D. Majumdar, Phys. Rev. **72**, 390 (1947).

[15] A. Papapetrou, Proc. Roy. Irish Acad. (Sect. A) **51**, 191 (1947).

[16] T. Assumpção, V. Cardoso, A. Ishibashi, M. Richartz, and M. Zilhão, Phys. Rev. D **98**, 064036 (2018).

[17] J. Shipley and S. R. Dolan, Class. Quant. Grav. **33**, 175001 (2016), arXiv:1603.04469 [gr-qc] .

[18] J. O. Shipley, *Strong-field gravitational lensing by black holes*, Ph.D. thesis, Sheffield U. (2019), arXiv:1909.04691 [gr-qc] .

[19] A. Bohn, W. Throwe, F. Hébert, K. Henriksson, D. Bunandar, M. A. Scheel, and N. W. Taylor, Class. Quant. Grav. **32**, 065002 (2015), arXiv:1410.7775 [gr-qc] .

[20] D. Bini, A. Geralico, G. Gionti, S. J., W. Plastino, and N. Velandia, Gen. Rel. Grav. **51**, 153 (2019), arXiv:1906.01991 [gr-qc] .

[21] D. Christodoulou and R. Ruffini, Phys. Rev. D **4**, 3552 (1971).

[22] G. W. Gibbons, Comm. Math. Phys. **44**, 245 (1975).

[23] I. Cabrera-Munguia, Physics Letters B **786**, 466 (2018).

[24] V. Manko and E. Ruiz, Physics Letters B **794**, 36 (2019).

[25] C. J. Ramírez-Valdez, H. García-Compeán, and V. S. Manko, Phys. Rev. D **102**, 024084 (2020).

[26] L. T. Sanches and M. Richartz, Phys. Rev. D **104**, 124025 (2021).

[27] S. Carroll, *Spacetime and Geometry: An Introduction to General Relativity* (Addison Wesley, 2004).

[28] A. A. Grib, Y. V. Pavlov, and V. D. Vertogradov, Mod. Phys. Lett. A **29**, 1450110 (2014), arXiv:1304.7360 [gr-qc] .

[29] G. Contopoulos, General Relativity and Gravitation **16**, 43 (1984).

[30] D. Christodoulou, Phys. Rev. Lett. **25**, 1596 (1970).

[31] J. B. Hartle and S. W. Hawking, Comm. Math. Phys. **26**, 87 (1972).

[32] O. Semerák and M. Basovník, Phys. Rev. D **94**, 044006 (2016).

[33] G. Denardo and R. Ruffini, Physics Letters B **45**, 259 (1973).

[34] J. Ryzner and M. Žofka, Class. Quant. Grav. **32**, 205010 (2015), arXiv:1510.02314 [gr-qc] .

[35] O. B. Zaslavskii, Mod. Phys. Lett. A **36**, 2150120 (2021), arXiv:2006.02189 [gr-qc] .

[36] A. Prasanna and N. Dadhich, Il Nuovo Cimento B (1971-1996) **72**, 42 (1982).

[37] F. de Felice, F. Sorge, and S. Zilio, Classical and Quantum Gravity **21**, 961 (2004).

[38] Z. Stuchlík, Bulletin of the Astronomical Institutes of Czechoslovakia **31**, 129 (1980).

[39] J. Levin and G. Perez-Giz, Phys. Rev. D **77**, 103005 (2008), arXiv:0802.0459 [gr-qc] .

[40] M. Bhat, S. Dhurandhar, and N. Dadhich, Journal of Astrophysics and Astronomy **6**, 85 (1985).

[41] S. Parthasarathy, S. Wagh, S. Dhurandhar, and N. Dadhich, The Astrophysical Journal **307**, 38 (1986).

[42] F. L. Dubeibe and J. D. Sanabria-Gómez, Phys. Rev. D **94**, (2016).

[43] M. Alcubierre, *Introduction to 3+1 Numerical Relativity* (2012).

[44] T. W. Baumgarte and S. L. Shapiro, *Numerical Relativity* (2010).

[45] T. W. Baumgarte and S. L. Shapiro, *Numerical Relativity: Starting from Scratch* (2021).

[46] F. H. Vincent, E. Gourgoulhon, and J. Novak, Classical and Quantum Gravity **29**, 245005 (2012).

[47] L. T. Sanches, Grlensing, https://github.com/lucass-carneiro/GRLensing (2022).

[48] D. R. Reynolds, D. J. Gardner, C. S. Woodward, and R. Chinomona, Arkode: A flexible ivp solver infrastructure for one-step methods (2022).

[49] G. Hart, S. Levy, and R. McLenaghan, *CRC Standard Mathematical Tables and Formulae, 31st Edition* (Chapman and Hall/CRC, 2002).

[50] R. Larson and R. P. Hostetler, *Precalculus with Limits: Student Text* (Houghton Mifflin, Boston, MA, 2006).

[51] C. Y. Young, *Precalculus* (John Wiley and Sons, Nashville, TN, 2010).

[52] J. D. Lawrence, *A catalog of special plane curves*, Dover Books on Mathematics (Dover Publications, Mineola, NY, 2014).

[53] M. F. Huq, M. W. Choptuik, and R. A. Matzner, Phys. Rev. D **66**, 084024 (2002).

[54] F. G. L. Armengol, L. Combi, M. Campanelli, S. C. Noble, J. H. Krolik, D. B. Bowen, M. J. Avara, V. Mewes, and H. Nakano, Astrophys. J. **913**, 16 (2021), arXiv:2102.00243 [astro-ph.HE] .

[55] L. Combi, F. G. L. Armengol, M. Campanelli, B. Ireland, S. C. Noble, H. Nakano, and D. Bowen, Phys. Rev. D **104**, 044041 (2021).

[56] R. F. Penna, Phys. Rev. D **91**, 084044 (2015).

[57] K. D. Kokkotas and B. G. Schmidt, Living Rev.Rel. **2**, 2 (1999).

[58] H.-P. Nollert, Class.Quant.Grav. **16**, R159 (1999).

[59] E. Berti, V. Cardoso, and A. O. Starinets, Class.Quant.Grav. **26**, 163001 (2009).

[60] R. A. Konoplya and A. Zhidenko, Reviews of Modern Physics **83**, 793 (2011).

[61] A. Buonanno, G. B. Cook, and F. Pretorius, Phys. Rev. D **75**, 124018 (2007), arXiv:gr-qc/0610122 .

[62] E. Seidel, Classical and Quantum Gravity **21**, S339 (2004).

[63] H. Ciftci, R. L. Hall, and N. Saad, Journal of Physics A: Mathematical and General **36**, 11807 (2003).

[64] H. T. Cho, A. S. Cornell, J. Doukas, T. R. Huang, and W. Naylor, Adv. Math. Phys. **2012**, 281705 (2012), arXiv:1111.5024 [gr-qc] .

[65] L. T. Sanches, Journal of Open Source Software **7**, 4077 (2022).

[66] J. Bezanson, A. Edelman, S. Karpinski, and V. B. Shah, SIAM Review **59**, 65 (2017).

[67] A. Jansen, Eur. Phys. J. Plus **132**, 546 (2017), arXiv:1709.09178 [gr-qc] .

[68] S. Fortuna and I. Vega, (2020), arXiv:2003.06232 [gr-qc] .

[69] C. O'Toole, R. Macedo, T. Stratton, and B. Wardell, Quasinormalmodes (2019).

[70] L. C. Stein, Journal of Open Source Software **4**, 1683 (2019), arXiv:1908.10377 [gr-qc] .

[71] L. A. H. Mamani, A. D. D. Masa, L. T. Sanches, and V. T. Zanchin, The European Physical Journal C **82**, 10.1140/epjc/s10052-022-10865-1 (2022).

[72] M. E. H. Ismail and N. Saad, Journal of Mathematical Physics **61**, 033501 (2020).

[73] L. T. Sanches, Quasinormalmodes.jl, `https://github.com/lucass-carneiro/QuasinormalModes.jl` (2022).

[74] E. Berti, Ringdown, https://pages.jh.edu/eberti2/ringdown/ (2022).

[75] F.-W. Shu and Y.-G. Shen, Phys. Lett. B **619**, 340 (2005), arXiv:gr-qc/0501098 .

[76] R. A. Konoplya, J. Phys. Stud. **8**, 93 (2004).

[77] H. T. Cho, Phys. Rev. D **68**, 024003 (2003), arXiv:gr-qc/0303078 .

[78] C. H. Chen, H. T. Cho, A. S. Cornell, and G. Harmsen, Phys. Rev. D **94**, 044052 (2016), arXiv:1605.05263 [gr-qc] .

[79] M. Shibata and T. Nakamura, Phys. Rev. D **52**, 5428 (1995).

[80] T. W. Baumgarte and S. L. Shapiro, Phys. Rev. D **59**, 024007 (1998).

[81] P. Diener, E. N. Dorband, E. Schnetter, and M. Tiglio, Journal of Scientific Computing **32**, 109 (2007).

[82] R. Haas, C.-H. Cheng, P. Diener, Z. Etienne, G. Ficarra, T. Ikeda, H. Kalyanaraman, N. Kuo, L. Leung, C. Tian, B.-J. J. Tsao, A. Wen, M. Alcubierre, D. Alic, G. Allen, M. Ansorg, F. G. L. Armengol, M. Babiuc-Hamilton, L. Baiotti, W. Benger, E. Bentivegna, S. Bernuzzi, T. Bode, G. Bozzola, S. R. Brandt, B. Brendal, B. Bruegmann, M. Campanelli, F. Cipolletta, G. Corvino, S. Cupp, R. D. Pietri, H. Dimmelmeier, R. Dooley, N. Dorband, M. Elley, Y. E. Khamra, J. Faber, T. Font, J. Frieben, B. Giacomazzo, T. Goodale, C. Gundlach, I. Hawke, S. Hawley, I. Hinder, E. A. Huerta, S. Husa, S. Iyer, L. Ji, D. Johnson, A. V. Joshi, W. Kastaun, T. Kellermann, A. Knapp, M. Koppitz, P. Laguna, G. Lanferman, F. Löffler, H. Macpherson, J. Masso, L. Menger, A. Merzky, J. M. Miller, M. Miller, P. Moesta, P. Montero, B. Mundim, P. Nelson, A. Nerozzi, S. C. Noble, C. Ott, R. Paruchuri, D. Pollney, D. Radice, T. Radke, C. Reisswig, L. Rezzolla, D. Rideout, M. Ripeanu, L. Sala, J. A. Schewtschenko, E. Schnetter, B. Schutz, E. Seidel, E. Seidel, J. Shalf, K. Sible, U. Sperhake, N. Stergioulas, W.-M. Suen, B. Szilagyi, R. Takahashi, M. Thomas, J. Thornburg, M. Tobias, A. Tonita, P. Walker, M.-B. Wan, B. Wardell, L. Werneck, H. Witek, M. Zilhão, B. Zink,

and Y. Zlochower, The einstein toolkit (2022), to find out more, visit http://einsteintoolkit.org.

[83] Cactus developers, Cactus Computational Toolkit ().

[84] Cactus developers, Cactus Computational Toolkit Prizes ().

[85] T. Goodale, G. Allen, G. Lanfermann, J. Massó, T. Radke, E. Seidel, and J. Shalf, in *Vector and Parallel Processing – VECPAR'2002, 5th International Conference, Lecture Notes in Computer Science* (Springer, Berlin, 2003).

[86] L. T. Sanches, Fieldperturbations (2021).

[87] P. V. P. Cunha, J. A. Font, C. Herdeiro, E. Radu, N. Sanchis-Gual, and M. Zilhão, Phys. Rev. D **96**, 104040 (2017).

[88] H. Witek, V. Cardoso, A. Ishibashi, and U. Sperhake, Phys. Rev. D **87**, 043513 (2013).